Comparative assessment of fast and thermal neutrons and gamma radiation protection qualities combined with mechanical factors of different borate-based glass systems

G. Lakshminarayana [a,*], H.O. Tekin [b,c], M.G. Dong [d], M.S. Al-Buriahi [e], Dong-Eun Lee [f,*], Jonghun Yoon [g,*], Taejoon Park [h,*]

[a] Intelligent Construction Automation Center, Kyungpook National University, 80, Daehak-ro, Buk-gu, Daegu 41566, Republic of Korea
[b] Medical Diagnostic Imaging Department, College of Health Sciences, University of Sharjah, Sharjah 27272, United Arab Emirates
[c] Istinye University, Faculty of Engineering and Natural Sciences, Computer Engineering Department, Istanbul 34396, Turkey
[d] Department of Resource and Environment, Northeastern University, Shenyang 110819, China
[e] Department of Physics, Sakarya University, Sakarya, Turkey
[f] School of Architecture, Civil, Environment and Energy, Kyungpook National University, 1370, Sangyeok-dong, Buk-gu, DaeGu 702-701, Republic of Korea
[g] Department of Mechanical Engineering, BK21 FOUR ERICA-ACE Center, Hanyang University, 55, Hanyangdaehak-ro, Sangnok-gu, Ansan-si, Gyeonggi-do 15588, Republic of Korea
[h] Department of Robotics Engineering, Hanyang University, 55 Hanyangdaehak-ro, Ansan, Gyeonggi-do 15588, Republic of Korea

ARTICLE INFO

ABSTRACT

Adequate shielding from ionizing radiations is essential in nuclear facilities because of such radiations' adverse effects on humans in the event of unwanted or accidental exposure. In the current work, for four distinct compositions of B_2O_3-Li_2O, Li_2O-Na_2O-K_2O-B_2O_3, Gd_2O_3-SiO_2-B_2O_3, and Bi_2O_3-Li_2O-ZnO-B_2O_3 glass systems, neutron and γ-ray attenuation competencies combined with elastic features have been examined for feasible nuclear radiation protection purposes. Σ_R (fast neutron removal cross-section) and for thermal energy neutrons σ_T (total cross-section) and *SP* (shielding percentage) were estimated. Comparably, in all samples, $50B_2O_3$-$10K_2O$-$40Li_2O$ (mol%) glass possesses larger Σ_R (=0.11755 cm^{-1}), whereas $25B_2O_3$-$37.5Si_2O$-$37.5Gd_2O_3$ (mol%) glass shows large σ_T (=646.171 cm^{-1}) and *SP* for thermal neutrons at minimal thickness, indicating the included Gd_2O_3's positive effect as element Gd has a high neutron absorption capacity. Employing the Phy-X/PSD program and MCNPX code, μ/ρ (mass attenuation coefficient) of all selected glasses is calculated for a γ-ray energy span of 0.015 – 15 MeV. Gd_2O_3 or Bi_2O_3 addition improved μ/ρ, and such increment is significant at low energies owing to PEA (photoelectric absorption) dominance and Gd or Bi *K*-edges. Also, for $15B_2O_3$-$10ZnO$-$5Li_2O$-$70Bi_2O_3$ (mol%) glass, μ/ρ has been derived by the WinXCOM program and FLUKA, Geant4, and PHITS codes, and a good accord between such simulated and theoretical μ/ρ outcomes is noticed following the calculated relative differences. Next, linear attenuation coefficient, effective atomic number and electron density, MFP (mean free path), TVL (tenth-value layer), HVL (half-value layer), and RPE (radiation protection efficiency) have also been evaluated. Comparatively, at 1.25, 0.662, and 0.2 MeV energies, $15B_2O_3$-$10ZnO$-$5Li_2O$-$70Bi_2O_3$ (mol %) sample possesses lower MFP and HVL than five SCHOTT AG commercial glass shields. Approximated RPE results affirmed all Gd_2O_3-SiO_2-B_2O_3 and Bi_2O_3-Li_2O-ZnO-B_2O_3 samples' potent absorption (almost 100%) ability for lower energy γ-rays. Moreover, equivalent atomic number, and by geometric progression fitting process, within energy 15 keV–15 MeV extent for ten different penetration depths at 1–40 mfp span buildup factors have been assessed. $15B_2O_3$-$10ZnO$-$5Li_2O$-$70Bi_2O_3$ (mol%) glass exhibits better gamma-ray shielding effectiveness in all chosen samples, specifying Bi_2O_3's favorable impact. Changes in photon shielding factors were interpreted following pair production, Compton scattering, and PEA processes. Later, elastic (Young's (*Y*), bulk (*K*), shear (*S*), and longitudinal (*L*)) moduli and Poisson's ratio values have been calculated for all inspected glasses. BC (bond compression) and M-M (Makishima–Mackenzie) models were utilized for such elastic traits reckoning. All *K*, *Y*, *S*, and *L* values' trends for binary B_2O_3-Li_2O glasses were identical in both BC and M-M models, and K_{bc} was

* Corresponding authors.
E-mail addresses: gandham@knu.ac.kr (G. Lakshminarayana), dolee@knu.ac.kr (D.-E. Lee), yooncsmd@gmail.com (J. Yoon), taejoon@hanyang.ac.kr (T. Park).

found to be raised from 73.63 to 89.89 GPa, while K_{M-M} increased from 75.35 to 180.53 GPa accordingly when Li_2O content improved from 9.6 to 39.9 mol% in the chemical composition.

Nomenclature

ρ	Density
Σ_R	Effective removal cross-section for fast neutrons
σ_{cs}	Coherent scattering cross-section
σ_{ics}	Incoherent scattering cross-section
σ_A	Absorption cross-section
σ_T	Total cross-section
μ/ρ	Mass attenuation coefficient
μ	Linear attenuation coefficient
Z_{eff}	Effective atomic number
N_{eff}	Effective electron density
HVL	Half-value layer
TVL	Tenth-value layer
MFP	Mean free path
RPE	Radiation protection efficiency
Z_{eq}	Equivalent atomic number
EBF	Exposure buildup factor
EABF	Energy absorption buildup factor
G–P	Geometric progression
PD	Penetration depth
BF	Buildup factor
M.W.	Molecular weight
V_m	Molar volume
CN	Coordination number
BC	Bond compression
M-M	Makishima–Mackenzie
$\dot{n}_c$	Average cross-link density
Ⅎ	Force constant
V_t	Total ionic packing density
G_t	Total dissociation energy
Y	Young's modulus
K	Bulk modulus
S	Shear modulus
L	Longitudinal modulus
σ	Poisson's ratio

Introduction

Relying on nuclear fission process of [235]U, after first power plant built commercially for electricity generation in 1954 in Obninsk, Russia, currently, 441 nuclear reactors are in operation in more than thirty countries supplying nearly 10% of the electricity globally (https://www. statista.com/statistics/267158/number-of-nuclear-reactors-in-opera tion-by-country/). Against fossil fuels, nuclear power functions as a clean energy source without producing greenhouse gas or CO_2 emissions at plant sites. Also, different radioisotopes (e.g., [198]Au, ^{137}Cs, ^{60}Co, ^{18}F, [131]Cs, ^{131}I, ^{99m}Tc, ^{90}Y, [201]T, etc.) could be made *via* neutron activation approach or charged particle-induced reactions at research reactors or cyclotrons for their utilization in the industry (agriculture and food sterilization) and nuclear medicine [1–4]. Regardless, nuclear power and radiopharmaceuticals generate various types of radiation like neutron, γ-rays, and *X*-rays. When exposed unwantedly (over extended periods) or accidentally, externally or internally, such radiations in humans could cause fatally adverse effects on their health [5]. In nuclear reactors, after the fission reaction, the formation of highly radioactive waste (spent nuclear fuel) is inevitable, which would cause devastating effects on the environment if not treated properly, as it emits high neutron radiation [6]. In this sense, for radiation workers, medical staff and the general public, and the environmental protection and well-being, at nuclear reactor sites, radiotherapy facilities, and spent-fuel transporting and storage sites for safe treatment, adequate shielding media is usually mandatory to minimize or block ionizing radiations [7,8]. Here, shields' performance depends on their chemical, physical, thermal, and mechanical factors and interacting radiation (neutron or γ) energy. Best composite shields show optimal competence against different radiations.

In nuclear reactors, nuclear waste storage sites, and radiation therapy centers, to contain radionuclides that emit radiations, usually, concrete and lead-based materials are utilized as barriers. Though concrete is favorable because of its cost-effectiveness, easy installation, better mechanical features, and capability to shield both neutron and γ radiation, it is opaque, leading visibility hard in nuclear facilities for the observation of radiation sources or humans. Also, over time, due to the H_2O loss from its pores, where initially H_2O content is essential for

neutrons attenuation, microcracks could form in its structure with bombarding radiations at elevated temperatures. Overall, this reduces the concrete's elastic aspects, density (ρ), and structural quality [9,10]. Similarly, disadvantages of lead are its high toxicity, inadequate mechanical durability, poor corrosion resistance, and limited capacity for neutron absorption [11]. On account of this, like other options, recently as barriers for ionizing radiation, researchers have studied and reported different types of polymer composites [12,13], alloys [14,15], steels [16–18], ceramics [19,20], lead-free glasses [21–23], and glass-ceramics [24,25]. In all such materials, glasses could be attractive for shielding nuclear radiation since they are optically transparent, nontoxic, and recyclable, where glasses can be fabricated in distinct shapes and large sizes with easy and low-cost synthesis approaches. Here thermal, structural, and elastic aspects of glasses can be effortlessly tuned by changing the chosen chemical compounds and preparation routes [22,23]. For neutron attenuation, all such features (thermal, structural, and elastic moduli) of glasses must be best in addition to thermal neutron absorption quality. In real radiation-emitting situations such as nuclear reactors' environments, neutron and γ-rays generally occur concomitantly, so designing media that attenuate or absorb neutrons and shield γ-rays at the same moment is critical.
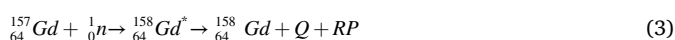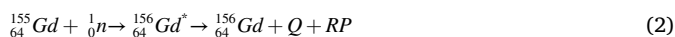
Neutrons (mass = 1.67493×10^{-27} kg) have no charge and exhibit high penetration capability. By colliding with atomic nuclei *via* fission, capture, and elastic and inelastic scatterings, neutrons ionize a material indirectly. Likewise, γ-rays having no mass and no charge could undergo pair production (PP), Compton scattering (CS), and photoelectric absorption (PEA) processes with a medium. Here dominant interaction probability depends on incident photon energy and the medium's Z/Z_{eff} (atomic number) and ρ. PEA mainly occurs at low energies in high Z/Z_{eff} materials, and at medium energies generally, the CS comes into play. Commonly, to attenuate high-energy *X*-rays or γ-rays, a denser substance with high Z/Z_{eff} is desirable. So, specific shield design heavily relies on the interactions between distinct radiations and the material utilized to protect against it. As stated in the "*Nomenclature*" assessing cautiously Σ_R and σ_{cs}, σ_{ics}, σ_A, and σ_T for fast and thermal neutrons, and μ/ρ, μ, MFP, TVL, HVL, RPE, N_{eff}, Z_{eff}, Z_{eq}, EABF, and EBF for γ-rays by correct formulae and simulation ways (*e.g.*, PHITS, Geant4, FLUKA, MNCPX, etc.) and/or theoretical means (*e.g.*, BXCOM, WinXCOM, XMuDat, Phy-X/PSD, Py-MLBUF, Phy-X/ZeXTRa, etc.) or experimentally is crucial for

applying a medium as a radiation attenuator [7,8,11–25].

On account of desirable features such as low cost, low melting point, expansive glass-forming ability, high optical transparency, finer mechanical and thermal stabilities with considerable viscosity, better third- and second-order optical nonlinearity, and moderate RE (rare-earth) elements solubility, B_2O_3-based glasses are regarded as attractive for industrial and scientific applications [11,26]. Usually, in B_2O_3 glasses superstructure units comprising explicit BO_3 and BO_4 units are dominant and the inclusion of network modifiers like alkali (Li_2O, Na_2O, K_2O, etc.) or alkaline metal oxides to vitreous B_2O_3 firstly causes an increase in boron (B) atoms CN (coordination number) from 3 to 4, instead of nonbridging oxygen atoms creation ($BO_3 \rightarrow BO_4$) [27]. Owing to the excellent fluxing and fluidizing efficacy of B_2O_3 and alkali oxides, such compounds are utilized in SiO_2 glass composition for highly radioactive nuclear waste immobilization, in which SiO_2 imparts exemplary chemical, mechanical, and thermal stabilities and corrosion resistance [28]. Further, B element having ^{10}B and ^{11}B isotopes, absorb neutrons effectively because of its high absorption cross-section area, σ_A (~767 b, 1 barn (b) = 10^{-28} m^2) while thermal neutron σ_A for ^{10}B = 3,835 b [29] due to the reaction [30,31]:

$$^{10}B + n_{thermal} \rightarrow {}^{11}Li + \alpha(1.47\ MeV) + {}^{7}Li(0.84\ MeV) \quad (1)$$
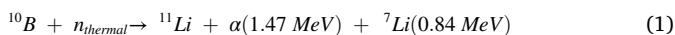
Besides, Gd_2O_3 ($\rho = 7.41$ g/cm^3, melting point ~2420 °C) is a RE oxide, and natural element Gd consists of a total of seven isotopes $^{152}_{64}Gd$, $^{154}_{64}Gd$, $^{155}_{64}Gd$, $^{156}_{64}Gd$, $^{157}_{64}Gd$, $^{158}_{64}Gd$, and $^{160}_{64}Gd$ respectively, where Gd has the largest σ_A (49,700 b) for thermal neutrons in all RE elements and also compared with B [29,31]. Here, neutrons can be captured by $^{155}_{64}Gd$ ($\sigma_A = 60,900$ b) and $^{157}_{64}Gd$ ($\sigma_A = 254,000$ b) [32] isotopes according to the reactions [32–34]:

$$^{155}_{64}Gd + {}^{1}_{0}n \rightarrow {}^{156}_{64}Gd^* \rightarrow {}^{156}_{64}Gd + Q + RP \quad (2)$$

$$^{157}_{64}Gd + {}^{1}_{0}n \rightarrow {}^{158}_{64}Gd^* \rightarrow {}^{158}_{64}Gd + Q + RP \quad (3)$$

where Q = exothermic value and RP = reaction products of nuclear and atomic structures radiative rearrangement.

Here (n, α) reaction of ^{10}B neutron capture creates α particles, and Gd captures neutron in (n, γ) reaction. Also, being a superior neutron attenuator, Gd has a relatively high Z (=64), offering itself as a self-γ absorber, where for spent-fuel storage, the shield must absorb both neutrons and γ-rays. However, element B liberates lesser energy secondary γ-rays than Gd. Both B and Gd elements' addition could be beneficial in fabricating thermal neutron shields or reaction control rods [35]. Being a heavy metal oxide, Bi_2O_3 (Bi (Z = 83), Bi^{3+}– low field strength and large polarizability), when added to a glass composition, it reduces glass transition temperature and enhances ρ and refractive index [36]. Also, depending on its included content, Bi_2O_3 could play a network modifier or former role, forming [BiO$_6$] or [BiO$_3$] units respectively in glass structures [11,21,36]. Further, Bi_2O_3, as non-toxic, may work as an alternative to PbO for designing γ-ray shields [11,20,21]. Likewise, counting on its added content (high or low), ZnO (non-toxic, inexpensive) also acts as a network former (ZnO$_4$ units) or modifier in a glass structure [37], where ZnO incorporation increases glass-forming span and decreases crystallization rates.

Latterly, with an aim to propose lead-free glasses as shields, El-Denglawey et al. [22] for $xMoO_3$–70TeO$_2$–(30–x)B$_2$O$_3$ (x = 0, 5, 10, 15, 20, 25, 30 mol%) samples, for 55B$_2$O$_3$–10ZnO–xY$_2$O$_3$–(35-x) Na$_2$O (x = 0, 2, 4 mol%) samples by Alrowaili et al. [23], Mahmoud et al. [38] for 50SiO$_2$-30Li$_2$O-1Gd$_2$O$_3$-(19-x)CdO-xEr$_2$O$_3$ (x = 0, 0.5, 1, 1.5, 2 mol %) glasses, for (70-x)WO$_3$-xGd$_2$O$_3$-30B$_2$O$_3$ (x = 17.5, 20, 22.5, 25, 27.5 mol%) samples by Kaewnuam et al. [39], Stalin et al. [40] for (60-x) TeO$_2$–10GeO$_2$–10ZnO–10Li$_2$O–10Bi$_2$O$_3$–xB$_2$O$_3$ (x = 0, 5, 10, 15, 20, 25 mol%) glasses, for 30Tl$_2$O$_3$ + 10Li$_2$O+(60-x)B$_2$O$_3$ + xSm$_2$O$_3$ (x = 0, 0.2, 0.4, 0.6 wt%) glass system by Saudi et al. [41], Saleh et al. [42] for 5Li$_2$O-(40-x) Na$_2$O-xZnO-55P$_2$O$_5$: 2 wt% (CdO + Te) (x = 0, 7, 14, 21, 28, 35, 40 mol%) glasses, for xBi$_2$O$_3$-(22-x)TiO$_2$-15V$_2$O$_5$-3Na$_2$O-60TeO$_2$

(x = 12, 14, 16, 18, 20 mol%) glass system by Zaid et al. [43], Rammah et al. [44,45] for (1 − x)MnO–29K$_2$O–70B$_2$O$_3$–xEr$_2$O$_3$ (x = 0, 0.2, 0.4, 0.6, 0.8, 1 mol%) samples and 45P$_2$O$_5$–(55-x)Na$_2$O–xCaO (x = 0, 10, 20, 30, 40, 50, 55 mol%) glasses, for five SiO$_2$-B$_2$O$_3$-Al$_2$O$_3$-Bi$_2$O$_3$-Na$_2$O-MgO-CaO (wt%) compositional glasses by Malidarre et al. [46], Aladailah et al. [47] for nine 20.15 [(2.038 + x)SiO$_2$-(1.457-x)Na$_2$O]-2.6P$_2$O$_5$-25.73CaO-1.22MgO (0 < x < 1, in steps of 0.125 mol%) glasses, for (90-x)P$_2$O$_5$–10SrO–xSb$_2$O$_3$ (x = 20, 25, 30, 35, 40 mol%) samples by Alharshan et al. [48], and Abouhaswa et al. [49] for 65P$_2$O$_5$ + 10Li$_2$O+ (25-x)BaO + xBi$_2$O$_3$ (x = 0, 5, 10, 15, 20, 25 mol%) samples, relevant nuclear radiation blocking competences have been assessed.

As main objectives of this work, for four kinds of B_2O_3-based glass systems in B_2O_3-Li$_2$O, Li$_2$O-Na$_2$O-K$_2$O-B$_2$O$_3$, Gd$_2$O$_3$-SiO$_2$-B$_2$O$_3$, and Bi$_2$O$_3$-Li$_2$O-ZnO-B$_2$O$_3$ compositions, related radiation shielding factors and by employing bond compression (BC) [50–52] and Makishima–Mackenzie (M-M) [53–55] models, standard mechanical features like Y (Young's), K (bulk), S (shear), and L (longitudinal) moduli, and σ (Poisson's ratio) are estimated. For neutrons Σ_R, σ_T, and SP (shielding percentage) are evaluated. Applying two different methods (MCNPX (v.2.6.0) [56] simulations and Phy-X/PSD software [57]), μ/ρ of all the inspected glasses is computed at energy 0.015 – 15 MeV span. WinXCOM program, FLUKA, Geant4, and PHITS codes have been also operated to derive μ/ρ for the highest ρ having sample in all compositions. MFP and HVL are contrasted with five commercial γ-ray glass shields' respective values. EBFs and EABFs are approximated utilizing G–P fitting perspective up to 40 MFP PDs. Current work's findings could be useful for the application of the glass types examined as neutron and γ-ray absorbers or shields in radioactive environments.

Materials and methods

For examined all B_2O_3-Li$_2$O, Li$_2$O-Na$_2$O-K$_2$O-B$_2$O$_3$, Gd$_2$O$_3$-SiO$_2$-B$_2$O$_3$, and Bi$_2$O$_3$-Li$_2$O-ZnO-B$_2$O$_3$ glass compositions, relevant measured ρ values have been collected from Refs. [58–61] respectively. Here for ease of use, such four borate-based glass systems are denoted as L1–L5, S1–S5, G1–G5, and B1–B4 accordingly. All selected glasses ρ as well as mol% and wt% of each composition are provided in Table 1 (i– iv) separately. From samples L1 to L5, G1 to G5, and B1 to B4 the ρ improves continually with increasing Li$_2$O, Gd$_2$O$_3$ + SiO$_2$, and Bi$_2$O$_3$ contents while from S1 to S5 sample ρ shows a nonlinear trend with Na$_2$O addition in place of Li$_2$O because of mixed alkali effect [59]. Computed individual M.W. is 65.814, 63.8265, 61.71975, 57.90375, and 53.76975 g/mol for L1, L2, L3, L4, and L5 samples, 56.187, 59.397, 62.607, 65.817, and 69.027 g/mol for S1, S2, S3, S4, and S5 glasses, 147.543, 154.626, 161.709, 168.792, and 175.875 g/mol for G1, G2, G3, G4, and G5 glasses, and 280.8365, 302.6405, 324.4445, and 346.2485 g/mol for B1, B2, B3, and B4 samples. Likewise, estimated V_m for L1–L5 glasses is 33.122, 31.044, 29.099, 25.792, and 23.49 cm^3/mol, for S1–S5 samples is 21.863, 22.845, 24.893, 26.015, and 27.392 cm^3/mol, for G1–G5 glasses is 35.096, 35.743, 36.619, 35.528, and 35.224 cm^3/mol, and for B1–B4 samples is 49.794, 52.179, 53.45, and 55.757 cm^3/mol respectively.

For all L1–L5, S1–S5, G1–G5, and B1–B4 samples, Σ_R is assessed by applying the relations [21] as:

$$\sum_R / \rho = \sum_i w_i \left(\sum_R / \rho \right)_i \quad (4)$$

where $w_i = i^{th}$ element's weight fraction, $(\sum_R/\rho)_i$ (cm^2/g) = i^{th} element's mass removal cross-section.

Since w_i is equivalent to Wi (partial density) by its ρ_s (density) as:

$$W_i = (w_i)(\rho_s) \quad (5)$$

eq. (4) becomes as:

Table 1

Chemical composition (mol%) and elements (wt%) present in the selected (i) binary B_2O_3-Li_2O glasses including their density [58] (ii) Li_2O/Na_2O-K_2O-B_2O_3 glasses including their density [59] (iii) Gd_2O_3-SiO_2-B_2O_3 glasses including their density [60], and (iv) Bi_2O_3-Li_2O-ZnO-B_2O_3 glasses including their density [61].

(i)

Glass code	Glass composition (mol%)		Elemental composition (wt%)			Density (g/cm³)
	B_2O_3	Li_2O	B	Li	O	
L1	90.4	9.6	29.7037	2.0252	68.2711	1.987
L2	85.4	14.6	28.9345	3.1759	67.8896	2.056
L3	80.1	19.9	28.0650	4.4765	67.4585	2.121
L4	70.5	29.5	26.3290	7.0733	66.5977	2.245
L5	60.1	39.9	24.1703	10.3024	65.5273	2.289

(ii)

Glass code	Glass composition (mol%)				Elemental composition (wt%)					Density (g/cm³)
	Li_2O	Na_2O	K_2O	B_2O_3	Li	Na	K	B	O	
S1	40	0	10	50	9.8836	0	13.9191	19.2429	56.9544	2.570
S2	30	10	10	50	7.0122	7.7418	13.1668	18.2029	53.8763	2.600
S3	20	20	10	50	4.4350	14.6898	12.4917	17.2696	51.1139	2.515
S4	10	30	10	50	2.1094	20.9599	11.8825	16.4273	48.6209	2.530
S5	0	40	10	50	0	26.6470	11.3299	15.6633	46.3598	2.520

(iii)

Glass code	Glass composition (mol%)			Elemental composition (wt%)				Density (g/cm³)
	Gd_2O_3	SiO_2	B_2O_3	Gd	Si	B	O	
G1	27.5	27.5	45	58.6204	5.2349	6.5948	29.5499	4.204
G2	30	30	40	61.0199	5.4492	5.5935	27.9374	4.326
G3	32.5	32.5	35	63.2091	5.6447	4.6799	26.4663	4.416
G4	35	35	30	65.2146	5.8238	3.8430	25.1186	4.751
G5	37.5	37.5	25	67.0585	5.9885	3.0736	23.8794	4.993

(iv)

Glass code	Glass composition (mol%)				Elemental composition (wt%)					Density (g/cm³)
	Bi_2O_3	Li_2O	ZnO	B_2O_3	Bi	Li	Zn	B	O	
B1	55	20	10	15	81.8557	0.9886	2.3281	1.1549	13.6727	5.64
B2	60	15	10	15	82.8636	0.6881	2.1603	1.0717	13.2163	5.80
B3	65	10	10	15	83.7361	0.4279	2.0151	0.9997	12.8212	6.07
B4	70	5	10	15	84.4986	0.2005	1.8883	0.9367	12.4759	6.21

$$\sum_R = \sum_i W_i \left(\sum_R / \rho \right)_i \tag{6}$$

where $(\sum_R/\rho)_i = i^{th}$ element's fast neutron removal cross-section, $Wi = i^{th}$ constituent's partial density.

Likewise, for thermal neutrons, σ_T is derived using the expression [11] as:

$$\sum (E) = N_A \rho \sum_i \frac{W_i}{M_i} \sigma_i(E) \tag{7}$$

where ρ (g/cm³) = sample's density, $(\sigma)_i(E)$ (in barn units) = i^{th} element's microscopic cross-section, $\sum E$ (cm^{-1}) = samples's macroscopic cross-section, $W_i = i^{th}$ element's mass fraction, $M_i = i^{th}$ element's atomic mass, N_A = Avogadro's number.

Next, for neutrons,

$$SP = (1 - exp^{-\sum \times t}) \times 100\% \tag{8}$$

where SP = shielding percentage, Σ = total macroscopic cross-section, t = glass thickness (cm).

Concerning vital γ-ray attenuation factors, related below formulae stated in Ref. [11] are utilized to compute them for studied glasses at 0.015 –15 MeV energy span.

$$\mu = \frac{-\ln\left(\frac{I}{I_0}\right)}{t} \tag{9}$$

where t = sample's thickness, I and I_0 = attenuated and original photon intensities.

$$(\mu/\rho)_{glass} = \sum_i w_i (\mu/\rho)_i \tag{10}$$

where $w_i = i^{th}$ element's weight fraction, $(\mu/\rho)_i = i^{th}$ element's μ/ρ.

$$Z_{eff} = \frac{\sum_i f_i A_i \left(\frac{\mu}{\rho}\right)_i}{\sum_j f_j \frac{A_j}{Z_j} \left(\frac{\mu}{\rho}\right)_j} \tag{11}$$

where f_i = fractional abundance, A_i = atomic weight, $Z_i = i^{th}$ element's atomic number.

$$N_{eff} = N_A \frac{nZ_{eff}}{\sum_i n_i A_i} = N_A \frac{Z_{eff}}{\langle A \rangle} \tag{12}$$

where $\langle A \rangle$ = mean atomic mass, N_A = Avogadro's number.

$$HVL = \frac{\ln(2)}{\mu} = \frac{0.693}{\mu} \tag{13}$$

$$TVL = \frac{\ln(10)}{\mu} = \frac{2.303}{\mu} \tag{14}$$

$$MFP = \frac{1}{\mu} \tag{15}$$

$$RPE = \left(1 - \frac{I}{I_0}\right) 100\% = (1 - e^{-\mu t}) \times 100\% \tag{16}$$

where μ = linear attenuation coefficient.

$$Z_{eq} = \frac{Z_1(\log R_2 - \log R) + Z_2(\log R - \log R_1)}{\log R_2 - \log R_1} \quad (17)$$

where Z_1 and Z_2 = atomic numbers of elements having ratios R_1 and R_2, R = ratio of the glasses at 0.015 – 15 MeV energy extent.

$$P = \frac{P_1(\log Z_2 - \log Z_{eq}) + P_2(\log Z_{eq} - \log Z_1)}{\log Z_2 - \log Z_1} \quad (18)$$

where P_1 and P_2 = G–P fitting factor values related to Z_1 and Z_2 at a particular energy.

EBFs and EABFs have been approximated by G–P fitting factors up to 40 mfp PDs by employing equations:

$$B(E, x) = 1 + \frac{b - 1}{K - 1}(K^x - 1) \quad \text{for} \quad K \neq 1 \quad (19)$$

$$B(E, x) = 1 + (b - 1)x \quad \text{for} \quad K = 1 \quad (20)$$

where $K(E, x)$ = photon-dose multiplication factor.

$$K(E, x) = cx^a + d\frac{\tanh(x/X_k - 2) - \tanh(-2)}{1 - \tanh(-2)} \text{for} x \leq 40 mfp \quad (21)$$

where E = incident photon energy, x = distance between source and detector, b = buildup factor at 1 mfp, and ($b, c, a, X_k,$ and d) = G–P fitting factors.

As it possesses the largest ρ, for glass B4, additionally μ/ρ is calculated using WinXCOM program [62] and PHITS (Particle and Heavy Ion Transport code System) [63], FLUKA (*FLUktuirende KAskade*) (http://www.fluka.org) [64,65], and Geant 4 (for GEometry ANd Tracking) [66–68] codes at twenty-five photon energy points for a contrast. Figs. S1 and S2 in SM (Supplementary Material) depict the adopted simulation geometries for respective MCNPX, PHITS, FLUKA, and Geant4 codes in this work. MCNPX is a 3-D GP (general-purpose) MC application code that operates advanced physics models and nuclear cross-section libraries. Fig. S1 (a) is modeled using an Input file consisting of Cell, Surface, and Data cards. Here we fixed Cell structures by describing elemental wt% and ρ and surfaces. Next, the surface's geometrical alignment for the inspected sample and its structure is defined. An energy span of 0.015–15 MeV was examined considering a point isotropic radioactive source to the DATA card area. Since it's not feasible straightway to acquire μ/ρ, following the shielded photon flux from the detector and accordingly Eq. (9) usage is essential. Here to record average flux in a point, the F4 tally is utilized. Simulations were performed for 10^8 particle histories. The outcomes revealed an associated inaccuracy for each track at <1%.

Likewise, PHITS is also a GPMC code that simulates at a wide energy span various particles' interactions with materials. Such code operates a large set of EM (electromagnetic) and nuclear models. In the Data card, classifications like parameters, medium, surface, cell, and source should be defined. Under narrow beam geometry, the source, sample, NaI detector, lead blocks, and collimators are aligned. The T-TRACK tally was utilized, and obtained results are at <0.1% uncertainty for 10^6 photon histories. For more details on employed PHITS code, readers could refer to our recent work [69]. Next, in brief, for FLUKA code, which is totally a combined particle physics MC kit, considered glass is placed in between the source and NaI detector, where both source and detector are covered by lead blocks to eliminate the secondary radiation particles. Here, the FLUKA input file contains the source, sample, detector, and their related dimensions. FLUKA default library was used to control all the EM and nuclear interplays in clarifying photon transmission through the sample. By enhancing the original count of colliding particles, the output's uncertainty could be minimized. Similarly, Geant4 is a C++-based MC code for simulating radiation-matter dynamics. The sample is placed between the source and detector that are shielded by lead slabs

and a collimator could be utilized to achieve a narrow-beam geometry.

Results and discussion

Nuclear radiation protection features

Neutrons

Usually, depending on their energy, neutrons are separated into different categories as fast (>0.1 MeV), intermediate (0.1–100 keV), epithermal (0.1–100 eV), and thermal (0.025 eV) neutrons [11,21]. In a nuclear reactor core, in a fission chain process, fast neutrons will be generated from enriched uranium by a slow neutron collision. Normally, neutrons undergo scattering and absorption mechanisms with substances relying on the energy, and in each interaction, they release distinct particles over wide energy spans [70]. *Via* the 'neutron moderation' step, using moderators like C, D_2O, and H_2O, fast neutrons energy is reduced to mean thermal energy. Here fast neutrons collide with light nuclei (*e.g.*, H) through elastic scatterings though it has a relatively large neutron σ_A owing to its affinity to create D_2O. As a prerequisite, a moderator should not absorb neutrons itself having a low neutron σ_A. For example, C, D_2O, and H_2O have σ_A 0.0035 b, 0.0013 b, and 0.66 b for neutrons accordingly [71]. With large ρ substances which possess heavy nuclei such as Bi or Pb, high energy neutrons interact *via* inelastic collisions. Generally, Σ_R reflects ~2/3 – 3/4 of σ_T. In current study for all examined samples, we considered $\sigma_T = \sigma_{cs} + \sigma_{ics} + \sigma_A$.

For all L1–L5, S1–S5, G1–G5, and B1–B4 glasses, related Σ_R computing processes and obtained Σ_R quantities are provided in Tables 2–5 respectively. With Li_2O addition in place of B_2O_3, from L1 to L5 sample, Σ_R continuously increased from 0.09228 cm^{-1} to 0.11239 cm^{-1} as related w_i and W_i improves, where Σ_R/ρ (cm^2/g) = 0.08399 and 0.05747 for Li and B (see Table 2). For S1, S2, S3, S4, and S5 glasses, individually 0.11755 cm^{-1}, 0.11388 cm^{-1}, 0.10578 cm^{-1}, 0.10244 cm^{-1}, and 0.09845 cm^{-1} is the derived Σ_R. Here at constant K_2O and B_2O_3 contents, Na_2O (Σ_R/ρ (cm^2/g) = 0.03225 for Na) inclusion instead of Li_2O clearly causes a reduction in Σ_R owing to an overall decrement of Σ_R of Li, B, O, and K (see Table 3). Likewise, separately 0.10186 cm^{-1}, 0.101 cm^{-1}, 0.09954 cm^{-1}, 0.10359 cm^{-1}, and 0.10548 cm^{-1} are the estimated Σ_R values for G1, G2, G3, G4, and G5 samples. From G1 to G3 sample Σ_R decreased, and later it increases for G4 and G4 glasses when

Table 2
Effective removal cross-sections for fast neutrons Σ_R (cm^{-1}) for all L1–L5 glasses.

Glass code	Element	Σ_R/ρ (cm^2/g)	Fraction by weight, w_i	Partial density (g/cm^3), W_i	Σ_R (cm^{-1})
	Li	0.08399	0.02025	0.04024072	0.00338001
	B	0.05747	0.29704	0.59021252	0.03391777
L1	O	0.04053	0.68271	1.35654676	0.05497845
	$\Sigma_R = 0.09227624$				
	Total Σ_R for glass 'L1' = 0.09228 cm^{-1}				
L2	Li	0.08399	0.03176	0.06529650	0.00548457
	B	0.05747	0.28935	0.59489332	0.03418676
	O	0.04053	0.67890	1.39581018	0.05656973
	$\Sigma_R = 0.09624106$				
	Total Σ_R for glass 'L2' = 0.09624 cm^{-1}				
	Li	0.08399	0.04477	0.09494657	0.00797502
	B	0.05747	0.28065	0.59525865	0.03420776
L3	O	0.04053	0.67459	1.43079479	0.05798759
	$\Sigma_R = 0.10017037$				
	Total Σ_R for glass 'L3' = 0.10017 cm^{-1}				
	Li	0.08399	0.07073	0.15879559	0.01333801
	B	0.05747	0.26329	0.59108605	0.03396797
L4	O	0.04053	0.66598	1.49511837	0.06059452
	$\Sigma_R = 0.10790049$				
	Total Σ_R for glass 'L4' = 0.1079 cm^{-1}				
	Li	0.08399	0.10302	0.23582194	0.01980782
	B	0.05747	0.24170	0.55325817	0.03179411
L5	O	0.04053	0.65527	1.49991990	0.06078911
	$\Sigma_R = 0.11239105$				
	Total Σ_R for glass 'L5' = 0.11239 cm^{-1}				

Table 3
Effective removal cross-sections for fast neutrons Σ_R (cm^{-1}) for all S1–S5 glasses.

Glass code	Element	Σ_R/ρ (cm^2/g)	Fraction by weight, w_i	Partial density (g/cm^3), W_i	Σ_R (cm^{-1})
	Li	0.08399	0.09884	0.25400852	0.02133540
	B	0.05747	0.19243	0.49454253	0.02841990
	O	0.04053	0.56954	1.46372808	0.05932232
S1	Na	0.03225	0.00000	0.00000000	0.00000000
	K	0.02368	0.13919	0.35772087	0.00847146
	$\Sigma_R = 0.11754909$				
	Total Σ_R for glass 'S1' = 0.11755 cm^{-1}				
	Li	0.08399	0.07012	0.18231720	0.01531370
	B	0.05747	0.18203	0.47327540	0.02719774
	O	0.04053	0.53876	1.40078380	0.05677130
S2	Na	0.03225	0.07742	0.20128680	0.00649140
	K	0.02368	0.13167	0.34233680	0.00810714
	$\Sigma_R = 0.11388129$				
	Total Σ_R for glass 'S2' = 0.11388 cm^{-1}				
	Li	0.08399	0.04435	0.11154025	0.00936880
	B	0.05747	0.17270	0.43433044	0.02495969
	O	0.04053	0.51114	1.28551459	0.05209964
S3	Na	0.03225	0.14690	0.36944847	0.01191453
	K	0.02368	0.12492	0.31416626	0.00744001
	$\Sigma_R = 0.10578268$				
	Total Σ_R for glass 'S3' = 0.10578 cm^{-1}				
	Li	0.08399	0.02109	0.05336782	0.00448262
	B	0.05747	0.16427	0.41561069	0.02388392
	O	0.04053	0.48621	1.23010877	0.04985414
S4	Na	0.03225	0.20960	0.53028547	0.01710145
	K	0.02368	0.11883	0.30062725	0.00711939
	$\Sigma_R = 0.10244152$				
	Total Σ_R for glass 'S4' = 0.10244 cm^{-1}				
	Li	0.08399	0.00000	0.00000000	0.00000000
	B	0.05747	0.15663	0.39471516	0.02268311
	O	0.04053	0.46360	1.16826696	0.04734780
S5	Na	0.03225	0.26647	0.67150440	0.02165569
	K	0.02368	0.11330	0.28551348	0.00676147
	$\Sigma_R = 0.09844807$				
	Total Σ_R for glass 'S5' = 0.09845 cm^{-1}				

Table 4
Effective removal cross-sections for fast neutrons Σ_R (cm^{-1}) for all G1–G5 glasses.

Glass code	Element	Σ_R/ρ (cm^2/g)	Fraction by weight, w_i	Partial density (g/cm^3), W_i	Σ_R (cm^{-1})
	B	0.05747	0.06595	0.27724539	0.01593247
	O	0.04053	0.29550	1.24227780	0.05034733
	Si	0.02814	0.05235	0.22007520	0.00619325
G1	Gd	0.01192	0.58620	2.46440162	0.02938528
	$\Sigma_R = 0.10185834$				
	Total Σ_R for glass 'G1' = 0.10186 cm^{-1}				
	B	0.05747	0.05594	0.24197481	0.01390558
	O	0.04053	0.27937	1.20857192	0.04898129
	Si	0.02814	0.05449	0.23573239	0.00663387
G2	Gd	0.01192	0.61020	2.63972087	0.03147577
	$\Sigma_R = 0.10099651$				
	Total Σ_R for glass 'G2' = 0.101 cm^{-1}				
G3	B	0.05747	0.04680	0.20666438	0.01187639
	O	0.04053	0.26466	1.16875181	0.04736745
	Si	0.02814	0.05645	0.24926995	0.00701484
	Gd	0.01192	0.63209	2.79131386	0.03328335
	$\Sigma_R = 0.09954203$				
	Total Σ_R for glass 'G3' = 0.09954 cm^{-1}				
	B	0.05747	0.03843	0.18258093	0.01049239
	O	0.04053	0.25119	1.19338469	0.04836578
	Si	0.02814	0.05824	0.27668874	0.00778644
G4	Gd	0.01192	0.65215	3.09834565	0.03694436
	$\Sigma_R = 0.10358898$				
	Total Σ_R for glass 'G4' = 0.10359 cm^{-1}				
	B	0.05747	0.03074	0.15346485	0.00881917
	O	0.04053	0.23879	1.19229844	0.04832176
	Si	0.02814	0.05989	0.29900581	0.00841448
G5	Gd	0.01192	0.67059	3.34823091	0.03992397
	$\Sigma_R = 0.10547938$				
	Total Σ_R for glass 'G5' = 0.10548 cm^{-1}				

Table 5
Effective removal cross-sections for fast neutrons Σ_R (cm^{-1}) for all B1–B4 glasses.

Glass code	Element	Σ_R/ρ (cm^2/g)	Fraction by weight, w_i	Partial density (g/cm^3), W_i	Σ_R (cm^{-1})
	Li	0.08399	0.00989	0.05575704	0.00468330
	B	0.05747	0.01155	0.06513636	0.00374319
	O	0.04053	0.13673	0.77114028	0.03125296
B1	Zn	0.01830	0.02328	0.13130484	0.00240224
	Bi	0.01030	0.81856	4.61666148	0.04752903
	$\Sigma_R = 0.08961073$				
	Total Σ_R for glass 'B1' = 0.08961 cm^{-1}				
	Li	0.08399	0.00688	0.03990980	0.00335222
	B	0.05747	0.01072	0.06215860	0.00357207
	O	0.04053	0.13216	0.76654540	0.03106674
B2	Zn	0.01830	0.02160	0.12529740	0.00229234
	Bi	0.01030	0.82864	4.80608880	0.04947920
	$\Sigma_R = 0.08976256$				
	Total Σ_R for glass 'B2' = 0.08976 cm^{-1}				
	Li	0.08399	0.00428	0.02597353	0.00218164
	B	0.05747	0.01000	0.06068179	0.00348720
	O	0.04053	0.12821	0.77824684	0.03154097
B3	Zn	0.01830	0.02015	0.12231657	0.00223780
	Bi	0.01030	0.83736	5.08278127	0.05232778
	$\Sigma_R = 0.09177540$				
	Total Σ_R for glass 'B3' = 0.09177 cm^{-1}				
	Li	0.08399	0.00201	0.01245105	0.00104582
	B	0.05747	0.00937	0.05816907	0.00334280
	O	0.04053	0.12476	0.77475339	0.03139939
B4	Zn	0.01830	0.01888	0.11726343	0.00214535
	Bi	0.01030	0.84499	5.24736306	0.05402217
	$\Sigma_R = 0.09195554$				
	Total Σ_R for glass 'B4' = 0.09195 cm^{-1}				

both Gd_2O_3 and Si_2O are enhanced in equal mol% instead of B_2O_3. Such a nonlinear trend in Σ_R is due to the total contributions of Σ_R of O, Si, and Gd though Σ_R of B is constantly reduced (see Table 4). This specifies that in a glass composition an appropriate mixture of light and high-Z elements could be beneficial in achieving a larger probability for fast neutrons scattering. Further, 0.08961 cm^{-1}, 0.08976 cm^{-1}, 0.09177 cm^{-1}, and 0.09195 cm^{-1} respectively are the obtained Σ_R quantities for B1, B2, B3, and B4 glasses. Here at fixed ZnO and B_2O_3 amounts, in place of Li_2O, Bi_2O_3 incorporation slightly improved Σ_R owing to enhancement in w_i, W_i, and Σ_R of Bi (see Table 5). It is known that material's ρ plays a decisive role regarding the scattering of fast neutrons $i.e.$, the greater the ρ, the better might be the Σ_R. Considering Tables 2–5 data, in all samples, S1 glass (Li: 9.8836 wt%, K: 13.9191 wt%, B: 19.2429 wt%, and O: 56.9544 wt%) possesses maximal Σ_R hinting at its better fast neutron attenuation ability, having $\rho = 2.57$ g/cm^3.

In comparison, Σ_R (=0.11755 cm^{-1}) of S1 glass is found to be greater than those of glass–ceramic S0 (=0.11357 cm^{-1}) [24], glass G4 (=0.1038 cm^{-1}) [40], glass G5 (=0.0805 cm^{-1}) [43], glass E5 (=0.1051 cm^{-1}) [44], ABS-0 glass (=0.1094 cm^{-1}) [46], Graphite (=0.0773 cm^{-1}) and H_2O (=0.1023 cm^{-1}) [72], and distinct concretes (OC (=0.0937 cm^{-1}), HSC (=0.0967 cm^{-1}), ILC (=0.0950 cm^{-1}), BMC (=0.1102 cm^{-1}), and IC = 0.1121 cm^{-1})) [73] respective quantities and lower than those of glass D (=0.1213 cm^{-1}) [11], glass F (=0.1206 cm^{-1}) [21], $55B_2O_3$–10ZnO–$4Y_2O_3$–$31Na_2O$ (mol%) glass (=0.144 cm^{-1}) [23], La5 glass–ceramic (=0.1316 cm^{-1}) [25], PLBB25 glass (=0.133 cm^{-1}) [49], BBLNi6 glass (=0.1383 cm^{-1}) [69], and concretes (SSC (=0.1247 cm^{-1}) and SMC (=0.1420 cm^{-1})) [73] related values.

Next, calculated σ_{cs}, σ_{ics}, σ_A, and σ_T values of all L1–L5, S1–S5, G1–G5, and B1–B4 samples for thermal neutrons are presented in Table 6 (i – iv) accordingly, while for 0.025 eV energy neutrons such values for all B, Li, Na, K, Gd, Si, Bi, Zn, and O elements present in the selected glasses are given in Table S1 in SM. Here σ_{cs} is dominant for elements Na, Si, Bi, Zn, and O (see Table S1). However, in all samples, σ_A caters highly to σ_T than those of σ_{cs} and σ_{ics} as σ_A is comparably greater than both of them. For L1–L5 glasses, σ_T varied at 25.5–26.645 cm^{-1} span, where sample L4 (B: 26.329 wt%, Li: 7.0733 wt%, and O: 66.5977

Table 6

Coherent scattering cross-section (σ_{cs}), incoherent scattering cross-section (σ_{ics}), absorption cross-section (σ_A), and total cross-section (σ_T) of all (i) L1–L5 (ii) S1–S5 (iii) G1–G5 and (iv) B1–B4 glasses for thermal neutrons attenuation. All derived values are in cm^{-1} units.

(i)				
Glass code	σ_{cs}	σ_{ics}	σ_A	σ_T
L1	0.333937746	0.059122938	25.45383177	25.847
L2	0.342099135	0.061566482	25.8069519	26.211
L3	0.34890942	0.063967972	26.00385166	26.417
L4	0.360843586	0.068669594	26.21604902	26.645
L5	0.357184451	0.071234971	25.07141397	25.500
(ii)				
Glass code	σ_{cs}	σ_{ics}	σ_A	σ_T
S1	0.339869923	0.048345984	21.13331414	21.521
S2	0.334004015	0.054805636	20.22729816	20.616
S3	0.314548867	0.058131935	18.56539477	18.938
S4	0.308675227	0.063124721	17.76767483	18.139
S5	0.300454123	0.06707259	16.87670486	17.244
(iii)				
Glass code	σ_{cs}	σ_{ics}	σ_A	σ_T
G1	0.539098266	1.45090546	480.7348269	482.725
G2	0.547169851	1.548914327	512.5858636	514.682
G3	0.551500352	1.633203534	539.9208763	542.105
G4	0.586386114	1.808413646	597.3102313	599.705
G5	0.609537845	1.95011127	643.6115578	646.171
(iv)				
Glass code	σ_{cs}	σ_{ics}	σ_A	σ_T
B1	0.26438784	0.010842993	3.124676277	3.400
B2	0.267212822	0.009296805	2.900555686	3.177
B3	0.275416458	0.00804993	2.752264378	3.036
B4	0.277980916	0.006733371	2.562227652	2.847

wt%) holds relatively a larger σ_T, indicating proper ratios of B and Li contributes well in attenuating thermal neutrons. Further, from sample S1 to S5, as expected, σ_T decreased (21.521 cm^{-1} to 17.244 cm^{-1}) as Li$_2$O is gradually replaced by Na$_2$O, where σ_T of Li and Na is 71.874 b and 3.81b respectively. Later, for G1–G5 glasses, an increase in SiO$_2$ and Gd$_2$O$_3$ contents in place of B$_2$O$_3$ enhanced absorption potency of thermal neutrons as σ_T changes from 482.725 cm^{-1} to 646.171 cm^{-1}. Such a rise is owing to a significantly larger σ_A value of Gd (=49,700 b) compared to B (=767 b). Similarly as the S1–S5 glasses trend, for B1–B4 samples also, σ_T reduced (3.4 cm^{-1} to 2.847 cm^{-1}) from glass B1 to B4 as Bi$_2$O$_3$ (Bi, σ_T = 9.1902 b) increases in place of Li$_2$O. Overall, in all examined glasses, following Table 6 data, G5 glass (Gd: 67.0585 wt%, Si: 5.9885 wt%, B: 3.0736 wt%, and O: 23.8794 wt%) shows a better capacity for thermal neutron absorption, possessing ρ = 4.993 g/cm^3, while sample B4 (ρ = 6.21 g/cm^3) owns the lowest σ_T. Comparably, sample G5 has extremely greater σ_T than those of glass A (=17.534 cm^{-1}) [11], sample A (=20.628 cm^{-1}) [21], glass G6 (=64.368 cm^{-1}) [40], and glass A (=23.251 cm^{-1}) [74] corresponding values.

Moreover, for 0.025 eV energy neutrons, SP values of all L1–L5, S1–S5, G1–G5, and B1–B4 glasses at distinct t (in mm) are shown in Fig. 1–4 accordingly. As can be seen from all such plots, the SP of all inspected samples enhances with t for neutrons. Such increment of SP occurs quickly for all glasses, and for all L1–L5 samples, at different t values SP is almost the same with a slight variation only, and it exceeds a value of 99% at t = 2 mm. Likewise, all S1–S5 glasses show >99% SP at t = 3 mm, where sample S1 possesses a higher SP in all S1–S5 samples as 88.38% at t = 1 mm and 99.99% at t = 5 mm. Thus, for all L1–L5 and S1–S5 glasses, respectively 2 mm and 3 mm thickness could be sufficient to effectively absorb or capture thermal neutrons. Concerning G1, G2, G3, G4, and G5 glasses, estimated SP at t = 0.001 mm is 38.29%, 40.23%, 41.85%, 45.1%, and 47.6% individually. Here, all G1–G5 samples exhibit >99% SP value just at t = 0.1 mm (100% SP at t = 0.5
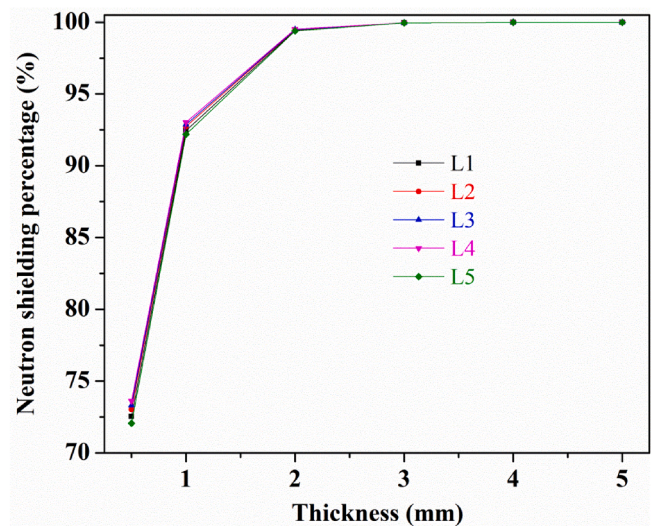

Fig. 1. Neutron shielding percentage of all L1–L5 glasses at different thickness (in mm) values.
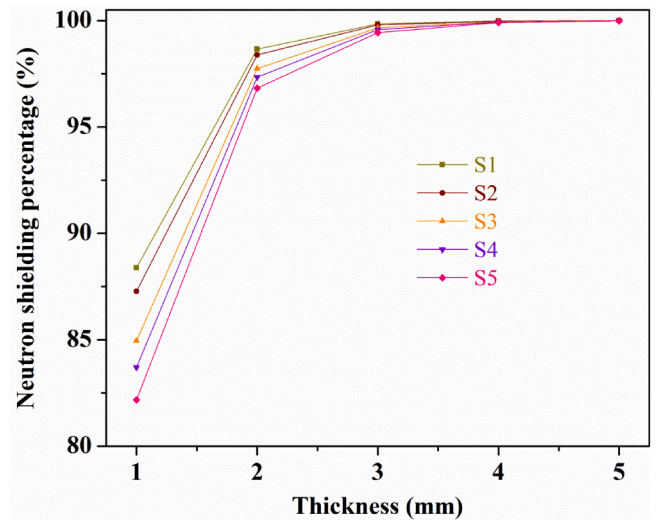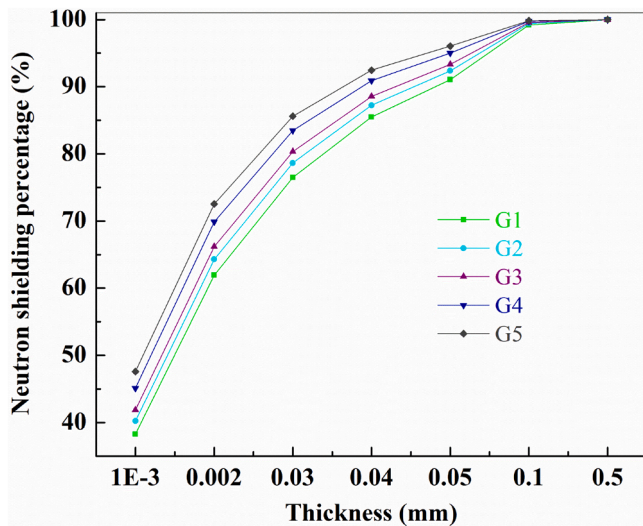

Fig. 2. Neutron shielding percentage of all S1–S5 glasses at different thickness (in mm) values.

mm) owing to contained element Gd in them. Later, in all B1–B4 samples SP is relatively better in glass B1 than the remaining ones, and a high t = 50 mm is necessary for all B1–B4 glasses to absorb efficiently thermal neutrons because of elements B and Li decrement in them though Bi increases and consequently ρ, as formers have greater micro cross-section than later one. In all studied samples, from Figs. 1 to 4, correlatively, glass G5 owns higher SP for thermal neutrons at minimal t than the rest of all the glasses owing to its superior σ_T.

γ-Rays

For all L1–L5, S1–S5, G1–G5, and B1–B4 samples by Phy-X/PSD derived μ/ρ values' changes at 0.015–15 MeV energy span are displayed in respective Fig. 5–8. Likewise, in Table S2 in SM, presented are the μ/ρ quantities computed by MCNPX code for all such glasses at the same energy range. In a medium, for realizing X-rays and γ-rays' penetration and diffusion μ/ρ is a vital trait, and usually, a larger μ/ρ specifies a better attenuation potential of a substance. Here μ/ρ does not rely on materials' ρ. For L1–L5 glasses, μ/ρ slightly reduced from L1 to L5 sample over the inspected energy span, for instance, at 0.015 MeV, 1.401 cm^2/g, 1.393 cm^2/g, 1.383 cm^2/g, 1.365 cm^2/g, and 1.342 cm^2/g

Fig. 3. Neutron shielding percentage of all G1–G5 glasses at different thickness (in mm) values.

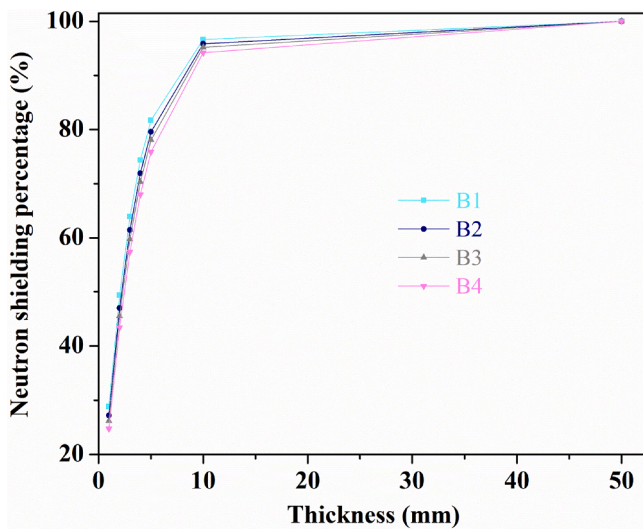**Fig. 4.** Neutron shielding percentage of all B1–B4 glasses at different thickness (in mm) values.
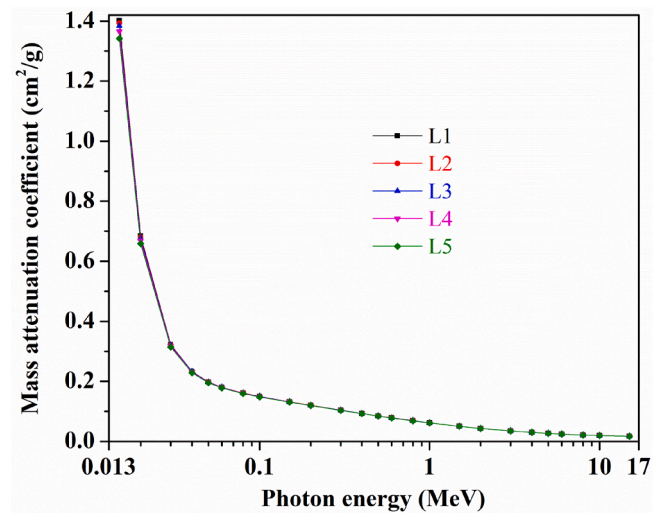

Fig. 5. Variation of mass attenuation coefficient with photon energy for all L1–L5 glasses.
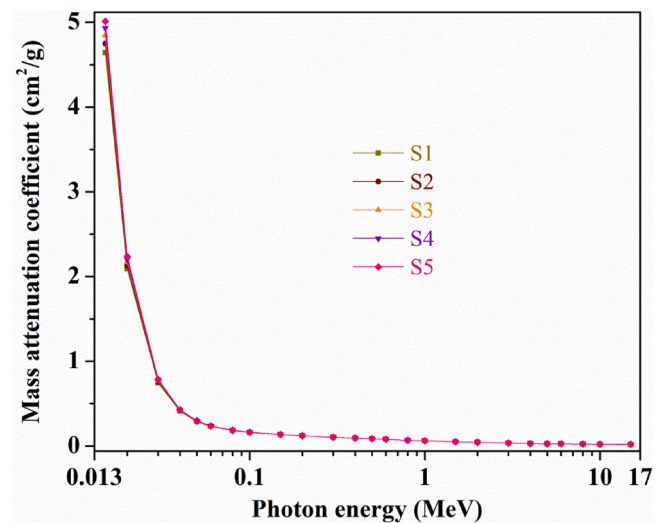
Fig. 6. Variation of mass attenuation coefficient with photon energy for all S1–S5 glasses.

are the μ/ρ values of L1, L2, L3, L4, and L5 glasses individually. But, for all S1–S5, G1–G5, and B1–B4 samples, S1 to S5, G1 to G5, and B1 to B4 glasses, μ/ρ minorly increased at any certain energy point. Such changes in μ/ρ could be clarified by the elements' variation owing to Li_2O/B_2O_3, Li_2O/Na_2O, $Gd_2O_3/SiO_2/B_2O_3$, and Bi_2O_3/Li_2O different ratios in L1–L5, S1–S5, G1–G5, and B1–B4 glasses correspondingly. Notably, Gd_2O_3 or Bi_2O_3 content rise in G1–G5 or B1–B4 samples enhances the total atomic weight of related glasses progressively, and as a consequence, μ/ρ increases, where being high-Z elements Gd or Bi possess a strong ability for photon absorption. For example, for 15 KeV energy photons, S5, G5, and B4 glasses have μ/ρ of 5.012 cm^2/g, 63.672 cm^2/g, and 99.751 cm^2/g respectively. Next, μ/ρ reduced with photon energy increment for all studied samples. As one can see from Figs. 5 to 8, at 15–40 keV range a sharp reduction in μ/ρ occurred owing to PEA dominance at such low energies, revealing that, the minimal the energy, the easy it is to absorb photons. After, above 0.04 MeV, with energy increment, the PEA effect decreases and CS process improves, resulting in increasing odds of CS, where CS weakly relies on Z. So, at an intermediate energy region, μ/ρ decrement is smoother compared to low energy range. At high energy region usually, as PP action dominates, for

G1–G5 and B1–B4 samples at above 6 MeV and 5 MeV energies, μ/ρ slightly improved. Also, high energy γ-rays are obstructed by glasses *via* repeated CS events, then scattered ones with lesser energy are ultimately absorbed by the PE effect. Here PEA, CS, and PP mechanisms are $\propto Z^{4-5}$, Z, and Z^2 separately [11]. Further, observed sharp hike at 60 keV and 100 keV (PEA control region) in μ/ρ of all G1–G5 and B1–B4 samples is because of Gd and Bi elements' K-edge located at 50.2 keV and 90.5 keV accordingly. In all examined glasses, from Figs. 5 to 8 and Table S2 data in SM sample B4 has comparably larger μ/ρ across all energies considered, suggesting its superior ability in attenuating γ-rays.

Moreover, for glass B4, μ/ρ is calculated using the WinXCOM program and Geant4, FLUKA, and PHITS codes for validation of μ/ρ outcome got from Phy-X/PSD or MCNPX. Fig. 9 depicts Phy-X/PSD and WinXCOM, and MCNPX, PHITS, FLUKA, and Geant4 codes derived μ/ρ versus photon energy comparison for glass B4. Table S3 in SM presents μ/ρ values of sample B4 obtained by WinXCOM and PHITS, FLUKA, and Geant4 codes along with RD% (relative difference) among them. As can be noticed from Fig. 9, μ/ρ results acquired by all six distinctive routes for glass B4 are adequately in good concord amidst themselves across all tested energy points. Especially, for estimated μ/ρ values by WinXCOM
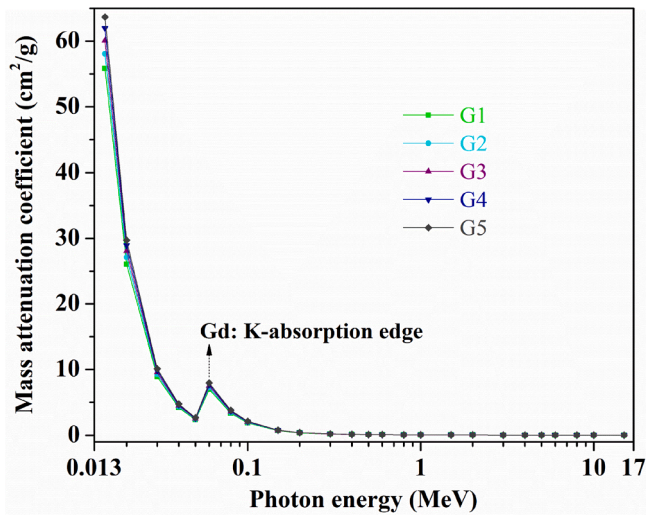
Fig. 7. Variation of mass attenuation coefficient with photon energy for all G1–G5 glasses.
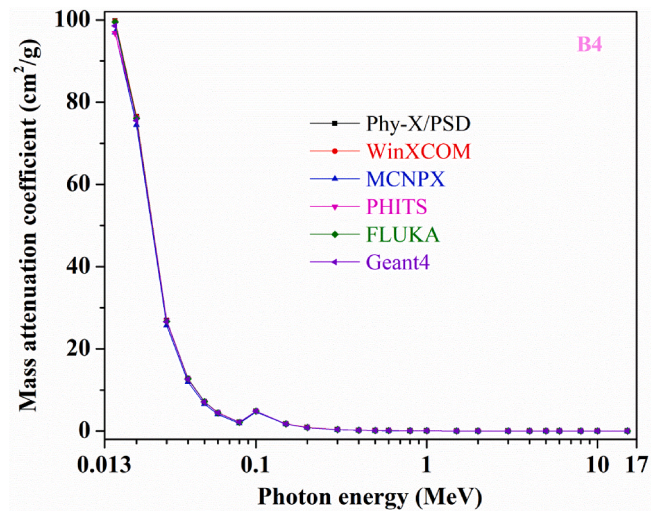

Fig. 9. Comparison of Phy-X/PSD and WinXCOM programs, MCNPX, PHITS, FLUKA, and Geant4 codes derived mass attenuation coefficients versus photon energy for glass B4.
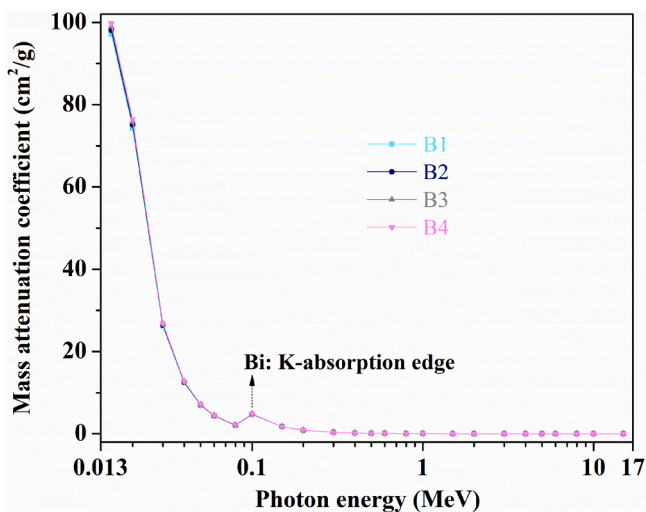

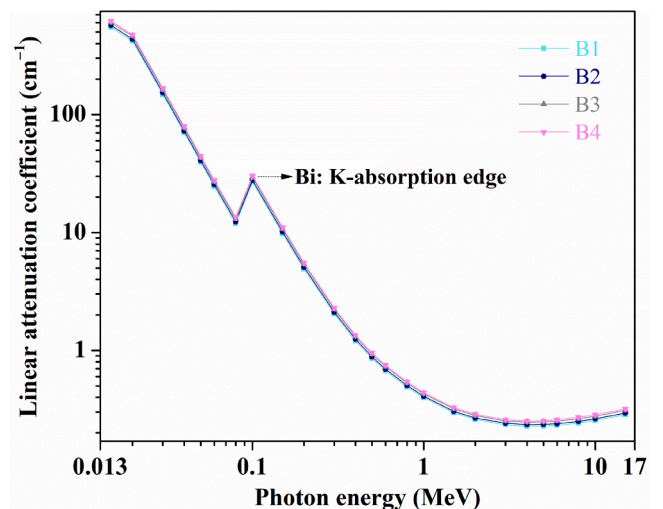**Fig. 8.** Variation of mass attenuation coefficient with photon energy for all B1–B4 glasses.

Fig. 10. Variation of linear attenuation coefficient with photon energy for all B1–B4 glasses.

and FLUKA RD is so small ($<$2%). For instance, for glass B4 for 0.04 MeV energy, 12.77 cm^2/g, 12.77 cm^2/g, 11.973 cm^2/g, 12.742 cm^2/g, 12.714 cm^2/g, and 12.61 cm^2/g are the computed μ/ρ values by Phy-X/PSD, WinXCOM, MCNPX, PHITS, FLUKA, and Geant4 individually. By FLUKA code, deduced μ/ρ of sample B4 for 1 MeV energy γ-ray is 0.06994 cm^2/g while for the identical energy photon 0.0599 cm^2/g and 0.0637 cm^2/g are only the related μ/ρ values for iron and concrete [75].

Fig. 10 illustrates μ values fluctuation with incident γ-ray energy for all B1–B4 glasses obtained by Phy-X/PSD, whereas similar μ variations for all L1–L5, S1–S5, and G1–G5 samples are exhibited in Figs. S3–S5 in SM correspondingly. As the μ depends on ρ, for all B1–B4 glasses, μ increases as the Bi_2O_3 amount improves from 55 to 70 mol%. A similar trend is also identified in μ for all L1–L5, S1–S5, and G1–G5 glasses with ρ enhancement. In all inspected samples, glass B4 having 84.4986 wt% Bi possesses the largest μ owing to its highest ρ. For instance, for 0.015 MeV energy, 547.46 cm^{-1}, 568.93 cm^{-1}, 600.79 cm^{-1}, and 619.45 cm^{-1} are respective μ results for B1, B2, B3, and B4 samples while for G1–G5 samples, separately 234.74 cm^{-1}, 251.19 cm^{-1}, 265.39 cm^{-1}, 294.37 cm^{-1}, and 317.91 cm^{-1} are such values at the same energy. Here, for S1–S5 glasses, alterations in μ are very less as ρ varies inconsequentially with Na_2O addition in place of Li_2O. For all B1–B4 glasses, the lowest μ

value is found for energy 4 MeV as 0.227 cm^{-1}, 0.234 cm^{-1}, 0.246 cm^{-1}, and 0.252 cm^{-1} individually. Interestingly, for L1–L5 and S1–S5 samples, with a continuous rise in energy, μ shows a similar drift, whereas for all G1–G5 and B1–B4 glasses at higher energies (above 6 MeV and 4 MeV) μ distinctly increases with the presence of elements Gd and Bi (high-Z) in them. Similarly as in the case of μ/ρ variations, here related PEA, CS, and PP processes that are $\propto E^{-3.5}$, E^{-1}, and log E are influential at lower, medium, and higher energy spans accordingly for observed μ fluctuations for all studied glasses. Particularly, μ in low energy area shows a strong downward trend for all glasses, where the biggest μ values are noticed in such region. So, photon blocking capacity greatly reduces due to the PE effect's strong energy reliance. In the case of greater energy regions, photons interact directly with nuclei, and eventually, the cross-section is larger than other energy spans. For all G1–G5 and B1–B4 samples, a quick rise identified in μ at 0.06 and 0.1 MeV is because of Gd and Bi K-edges separately. For any certain energy, changes between μ values are larger than those of μ/ρ because of variation in the samples' mass ρ as μ is highly reliant on shifts in ρ.

For all L1–L5, S1–S5, G1–G5, and B1–B4 glasses, Figs. S6–S9 and Figs. S10–S13 in SM exhibit respective Z_{eff} and N_{eff} variations with γ-ray

energy. Z_{eff} is a vital factor in elucidating radiation shields' attenuating abilities. Basically, Z_{eff} and N_{eff} rely on photon energy and individual elements comprised in the samples' compositions. Here, for all examined samples, both Z_{eff} and N_{eff} patterns show a similar drift with energy. All samples have the maximal Z_{eff} and N_{eff} values at lower energies. Primarily, Z_{eff} improved the same as μ/ρ with Gd_2O_3 and Bi_2O_3 content increment from G1 to G5 and B1 to B4 glass, whereas N_{eff} exhibits an opposite movement to Z_{eff} fluctuations for such glasses. Generally, in glasses, the inclusion of high-Z elements like Gd or Bi enhances Z_{eff} of them. Considering L1–L5 and S1–S5 samples, glass L1 and sample S5 (except for energies 0.015 and 0.2 MeV) possesses the largest Z_{eff} quantities, while N_{eff} values are the highest for L5 sample up to 0.05 MeV (PEA control span) in L1–L5 glasses, and up to 0.1 MeV for S1 glass in S1–S5 samples. Comparably, in all studied samples, glass B4 holds the biggest Z_{eff}, and sample G1 owns the highest N_{eff} values. For example, for 15 keV energy, 7.5, 13.66, 58.95, and 79.08 are the calculated related Z_{eff} values for L1, S1, G5, and B4 glasses, while 3.48×10^{23}, 5.86×10^{23}, 10.48×10^{23}, and 7.22×10^{23} electrons/g are corresponding computed N_{eff} quantities for L5, S1, G1, and B1 samples. Both Z_{eff} and N_{eff} and their ranges at distinct energy spans (i.e., minimal, medium, and greater) could be affected by the PEA, CS, and PP mechanisms. At intermediate and higher energy regions, for each sample of L1–L5 and S1–S5 glasses, changes in Z_{eff} and N_{eff} are negligible with an energy rise, whereas for G1–G5 and B1–B4 samples, Z_{eff} and N_{eff} quantities considerably increase at greater energies. For instance, for B4 glass, Z_{eff} is 35.12 (lowest) and 55.29 for 1.5 MeV and 15 MeV energies, while for the G1 sample individual N_{eff} is 2.81×10^{23} and 4.67×10^{23} electrons/g for the same energies. As sample B4 owns the largest Z_{eff} it could be regarded as a superior attenuator for photons.

Figs. 11 and 12 shows calculated HVL, TVL, and MFP disparities with γ-ray energy for L5, S5, G5, and B4 glasses accordingly. Here all such parameters depend on the incident energy similar to μ/ρ and a specific compositional glass. For a medium's utilization in medical diagnostics and radiation environments as a shield, TVL and HVL are critical in determining its thickness needed to reduce initial photons' intensity by $1/10^{th}$ and $½$, and MFP reflects the average length X-ray or γ-ray voyages before a collision with atoms in it. As mentioned in Section 2, one can see that μ and MFP, TVL, and HVL have an inverse correlation. So, the larger the μ, the lesser the thickness required to absorb radiations, and lower quantities of MFP clear indicate better shielding aspect. In other words, the greater the radiation intensity or energy, the thicker the shield must be. From Figs. 11 and 12, one can notice that with energy rise from 15 keV to 15 MeV, L5 and S5 samples' HVL, TVL, and MFP increases continually showing a similar drift, where the sample S5 has such values lower than L5 glass at any certain energy point. But for G5 and B4 glasses, HVL, TVL, and MFP, following the same trend, enhance with improving energy up to a specific point only, and then reduce later up to 15 MeV. Fig. 11 reveals that for all glasses minimal thicknesses are enough to decrease low energy photons (PEA dominance region) intensity to 50% owing to their poor penetrating capacity, while at greater energy spans, to absorb 50% photons a higher thickness is mandatory as at such larger energies both CS and PP processes generate secondary photons. For instance, for 0.015 MeV energy, respectively 0.22 cm, 0.05 cm, 0.002 cm, and 0.001 cm are the HVL for L5, S5, G5, and B4 glasses, whereas for 6 MeV energy, 12.48 cm, 10.79 cm, 3.99 cm, and 2.68 cm are the corresponding HVL for the same samples. For photons of 60 and 20 keV energies that are employed in CT scannings and Mammography, for B4 glass 0.025 cm and 0.0015 cm are the HVL values. It can be observed that TVL > HVL and MFP > HVL for the same energy for all samples. Further, Fig. 12 clarifies that higher energy photons' collide less with samples and needs larger thickness glasses to improve the possibility of interactions between photons and glass. For example, for 6 MeV energy, for samples L5, S5, G5, and B4, 18.01 cm, 15.57 cm, 5.75 cm, and 3.87 cm are the estimated MFP accordingly. In all samples, correlatively, B4 glass holds minimal MFP, TVL, and HVL for any considered energy point as it possesses the highest μ and ρ. So, it is
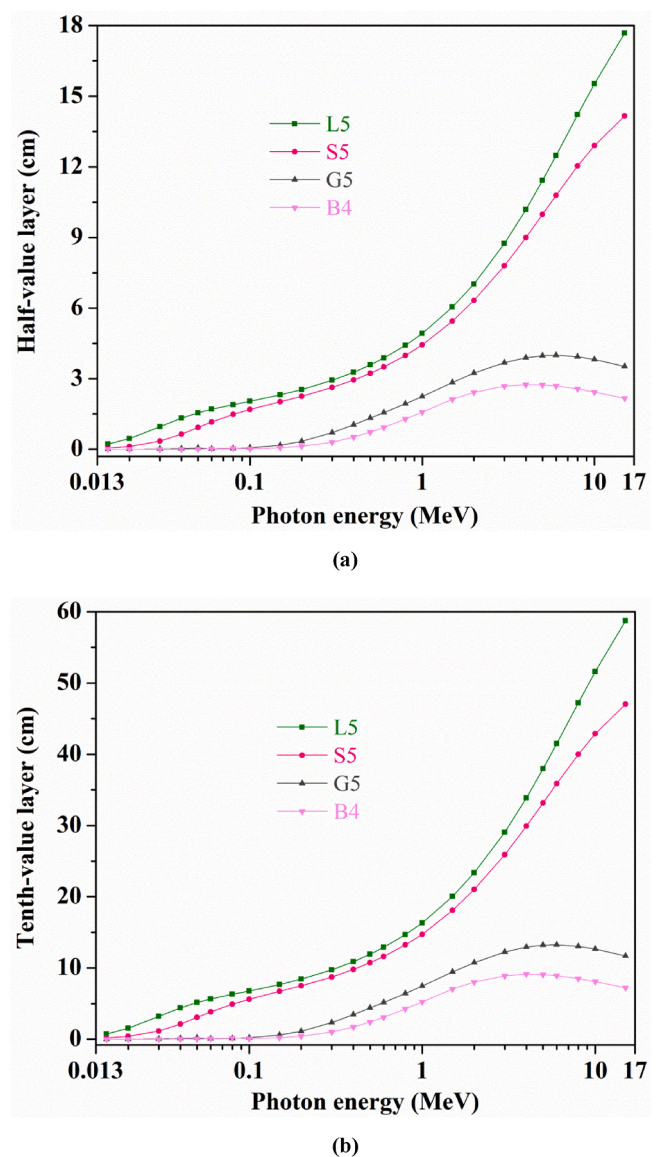
(a)

(b)

Fig. 11. Variations of (a) half-value layer and (b) tenth-value layer with photon energy for L5, S5, G5, and B4 glasses.

obvious that for improving photon shielding qualities and for less physical space requirement, it is beneficial to add heavy elements like Bi in glass compositions in higher quantities.

Moreover, at 1.25, 0.662, and 0.2 MeV energies, Fig. 13 (a) and (b) separately depicts HVL and MFP comparison of glass B4 to related values of SCHOTT AG RS 520, RS 360, RS 323 G19, RS 253 G18, and RS 253 commercial glass shields [76]. For all three energies, sample B4 exhibits lesser MFP and HVL than all those five commercial glasses' related values. For instance, for 0.662 MeV energy, glass B4 has an HVL of 1.044 cm, whereas for RS 520 glass it is 1.386 cm for such energy point, revealing that to decrease 662 keV γ-rays intensity to $½$, ~1.327 times lower thickness glass B4 is appropriate than sample RS 520. Next, for 1250 keV energy, 2.73 cm and 3.33 cm are MFP values for glasses B4 and RS 520 individually, indicating that γ-rays interaction odds will be the same in sample B4 even with ~ 1.219 times lesser thickness than in glass RS 520 for this energy.

For all B1–B4 glasses ($t = 1$ cm), Fig. 14 displays changes in RPE at 0.015–15 MeV energy span while similar RPE deviations for all L1–L5, S1–S5, and G1–G5 glasses are showcased in Figs. S14–S16 in SM separately. Generally, RPE characterizes the amount of energy stored inside a
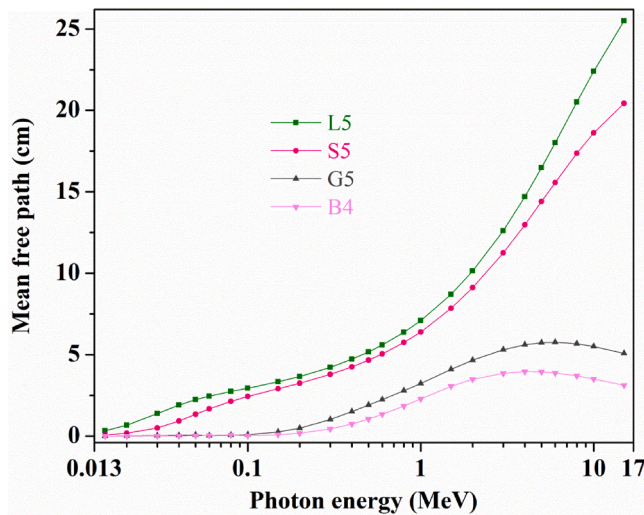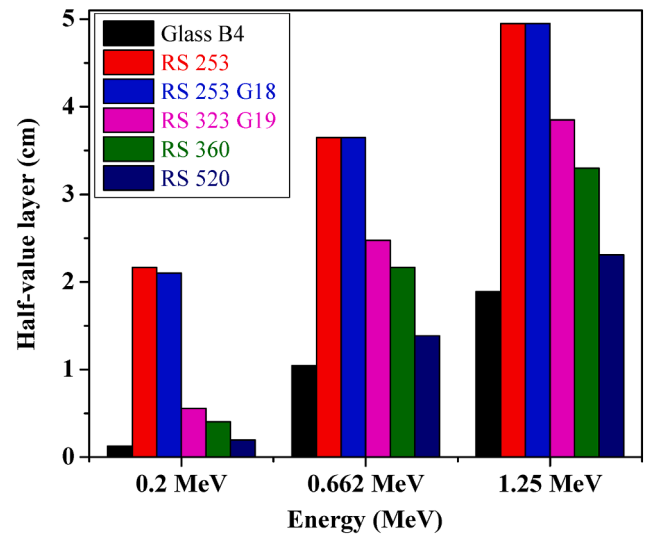
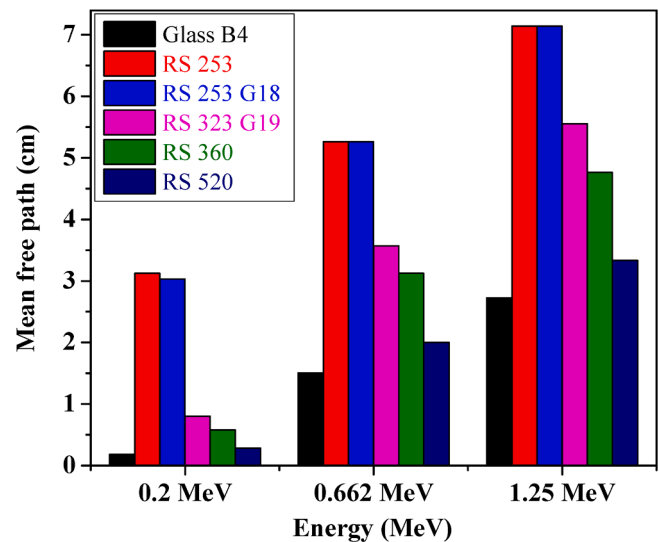**Fig. 12.** Variation of the mean free path with photon energy for L5, S5, G5, and B4 glasses.

(a)

(b)

Fig. 13. Comparison of (a) half-value layer and (b) mean free path of the glass B4 with some commercial shielding glasses.

medium. Similar to μ alterations, for all samples, RPE is also reduced with increasing energy.

Here, energy rise causes a reduction in the retained energy inside glasses along the travel path of photons, and RPE declines in an exponential route. For L1–L5 and S1–S5 glasses, RPE shows an identical drift while for G1–G5 and B1–B4 samples, RPE exhibits the same movement with energy. All the inspected samples demonstrate the highest RPE for lower energy γ-rays than greater energy ones. For instance, for 0.015 MeV energy, for L5, S5, G5, and B4 glasses 95.36%, 99.99%, 100%, and 100% are the derived RPE values individually. At explored energy span, in all glasses, sample B4 owns a greater RPE, as it has higher Z and ρ. From Fig. 14 and Figs. 14–16, one can see that Gd and Bi contribute more to occur γ-ray collisions with glasses than light elements such as Li and Na in them. For example, in B1–B4 samples, the substitution of Li_2O by Bi_2O_3 causes a slight increase in the γ-ray interaction cross-section, leading to a bigger resistance for incoming photons. Consequently, interactions between photons and atoms comprising in glass enhance, causing a decrement in photons' number penetrating the glass. So, for photons, the higher the Z of the shield, the better the absorption. Further, for 15 MeV energy, glass B4 possesses 27.35% RPE, meaning the remaining 72.65% photons of 15 MeV energy could pass through it. Here, a larger thickness (> 1 cm) sample B4 could attenuate a higher % of 15 MeV energy photons, i.e., the greater the thickness, the higher the PRE.

For L1, S5, G5, and B4 glasses, Fig. 15 (a-d) and (e-h) illustrate computed EBFs and EABFs variations with γ-ray energy at ten distinct PDs from 1 to 40 mfp correspondingly. Also for all such glasses, Fig. S17 in SM depicts calculated Z_{eq} changes with energy where Z_{eq} of an attenuator could be assessed only by the Incoherent scattering [77]. Such Z_{eq} quantities are utilized for BUFs (buildup factors) evaluation. Here, BUF offers an insight on secondary γ-rays created in a medium and energy stored inside it. Commonly, BUF >1 and depends on t and Z/Z_{eff} of an absorber, incident energy, mfp, and source design [11]. During interaction events, when scattering cross-section falls or absorption is superior, BUFs could reach or surpass unity. So, accurate BUFs quantification helps in designing precisely γ-ray attenuators for their use at nuclear reactors sites. There exist two kinds of BUFs: EBF and EABF. Generally, for a shield, the larger the EBFs and EABFs, the minimal the γ-ray attenuation or absorption capacity. As can be noticed from Fig. 15, with energy and PD, EBFs and EABFs movement for L1 and S5 glasses show a similar trend while for G5 and B4 samples such values vary in an identical trend. Owing to the presence of Gd: K-edge and Bi: L1- and K-edges, a quick hike in EBFs and EABFs at 0.06 MeV in the G5 sample and

0.03 and 0.1 MeV in B4 glass is identified accordingly. Moreover, as expected, at such specific energy points, a constant rise in γ-rays BUFs is observed with PD. At related 0.08–0.1 MeV and 0.08–0.15 MeV ranges for L1 and S5 samples, EBFs and EABFs have attained maximal values, and then with increasing energy, such quantities continually reduced up to 15 MeV. For G5 and B4 glasses, with the omission of sharp rises at respective elemental absorption edges, EBFs and EABFs are trifling at energy 0.015–0.2 MeV span since lesser energy γ-rays are completely attenuated or absorbed by such samples because of PEA control. After that, the CS process becomes dominant, and EBFs and EABFs increase at intermediate energy span, owing to the occurrence of photons' multiple scatterings in G5 and B4 samples. Next at higher PDs (10–40 mfp) and energies as PP mechanism governs BUFs are improved additionally in such glasses. Generally, a hike in PD causes an increase in scattered γ-rays created by electron–positron annihilation. Photons buildup mostly occurs at greater mfp, mainly for thicker samples and a higher diversity of colliding X-rays or γ-rays. But, BUF alterations are insignificant at 1 and 2 mfp at greater energies for G5 and B4 glasses though usually one can anticipate a continual rise in BUFs with a hike in mfp. In all glasses, sample B4 possesses minimal BUFs at all examined γ-ray
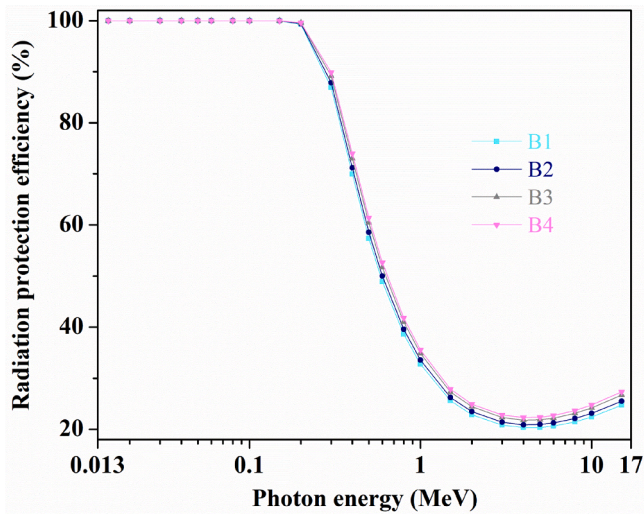
Fig. 14. Variation of radiation protection efficiency with photon energy for all B1–B4 samples.

energies as collision chances of such incoming rays is considerably increased due to the high amount of Bi (=84.4986 wt%) in it. Later, from Fig. S17 one can see that at all considered energies, Z_{eq} changes for L1 and S5 glasses are marginal whereas G5 and B4 samples at CS action dominating range (medium energies) own higher Z_{eq} values. In all samples, glass B4 holds larger Z_{eq} varying at 42.94 (lowest, for 40 keV) – 76.18 (highest, for 1 MeV) followed by G5 sample (Gd: 67.0585 wt%). So, Bi_2O_3 or Gd_2O_3 content rise in glasses enhances their attenuation ability for photons.

Mechanical traits

A glass can serve its purpose effectively as a radiation shield only when it has better mechanical features and superior radiation attenuation factors. Here for glasses, larger values of elastic moduli imply their high rigidity. For all L1–L5, S1–S5, G1–G5, and B1–B4 glasses, using both BC and M-M models [50–55], mechanical factors (K, Y, S, and L) and σ are computed. Separately in Table 7 (i) and (ii), all relevant utilized parameters and formulae of such models for calculation processes are presented. In all studied samples, for existing oxides like B_2O_3, Li_2O, Na_2O, K_2O, Gd_2O_3, SiO_2, Bi_2O_3, and ZnO, n_c (cross-link density per cation), n_f (CN per cation), f (stretching force constant), and r (bond
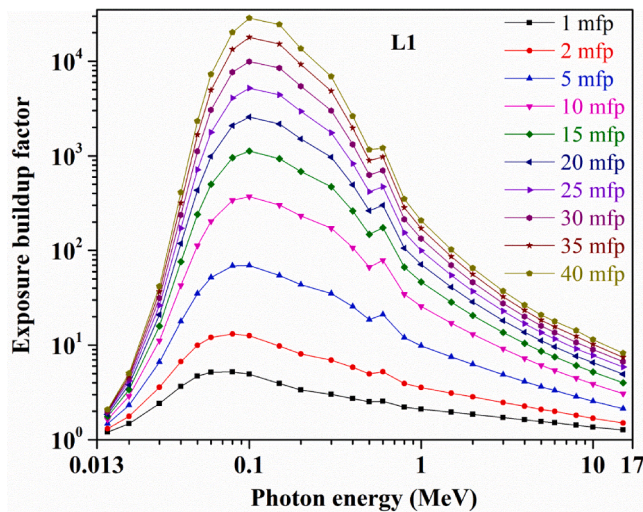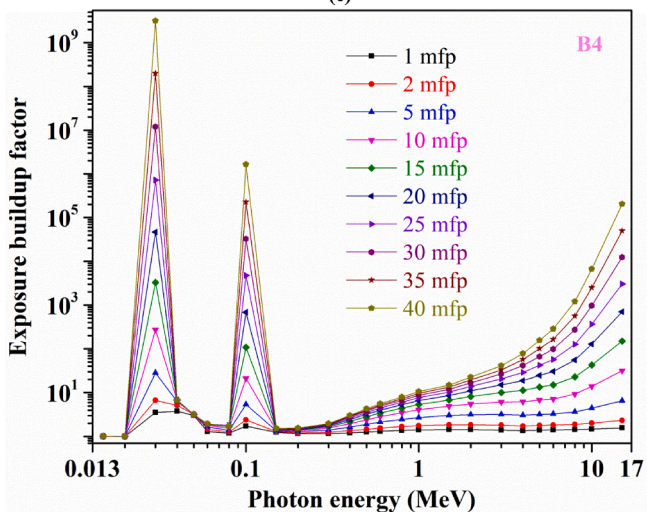

(a)
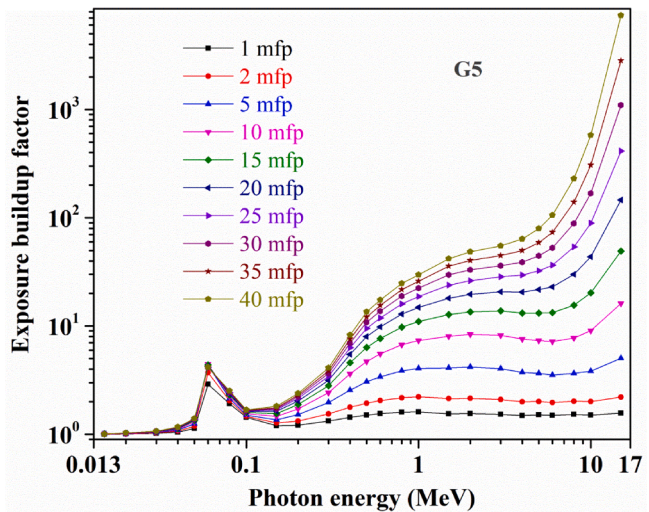
(c)
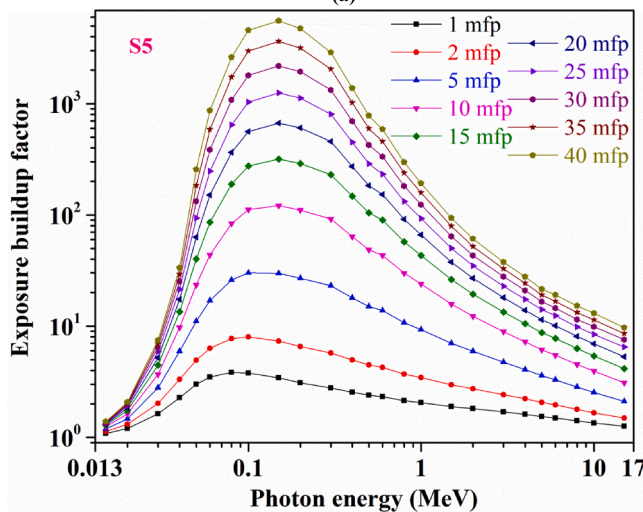
(b)

(d)

Fig. 15. Variations of (a-d) exposure buildup factor and (e-h) energy absorption buildup factor with photon energy at different mean free paths for glasses L1, S5, G5, and B4.
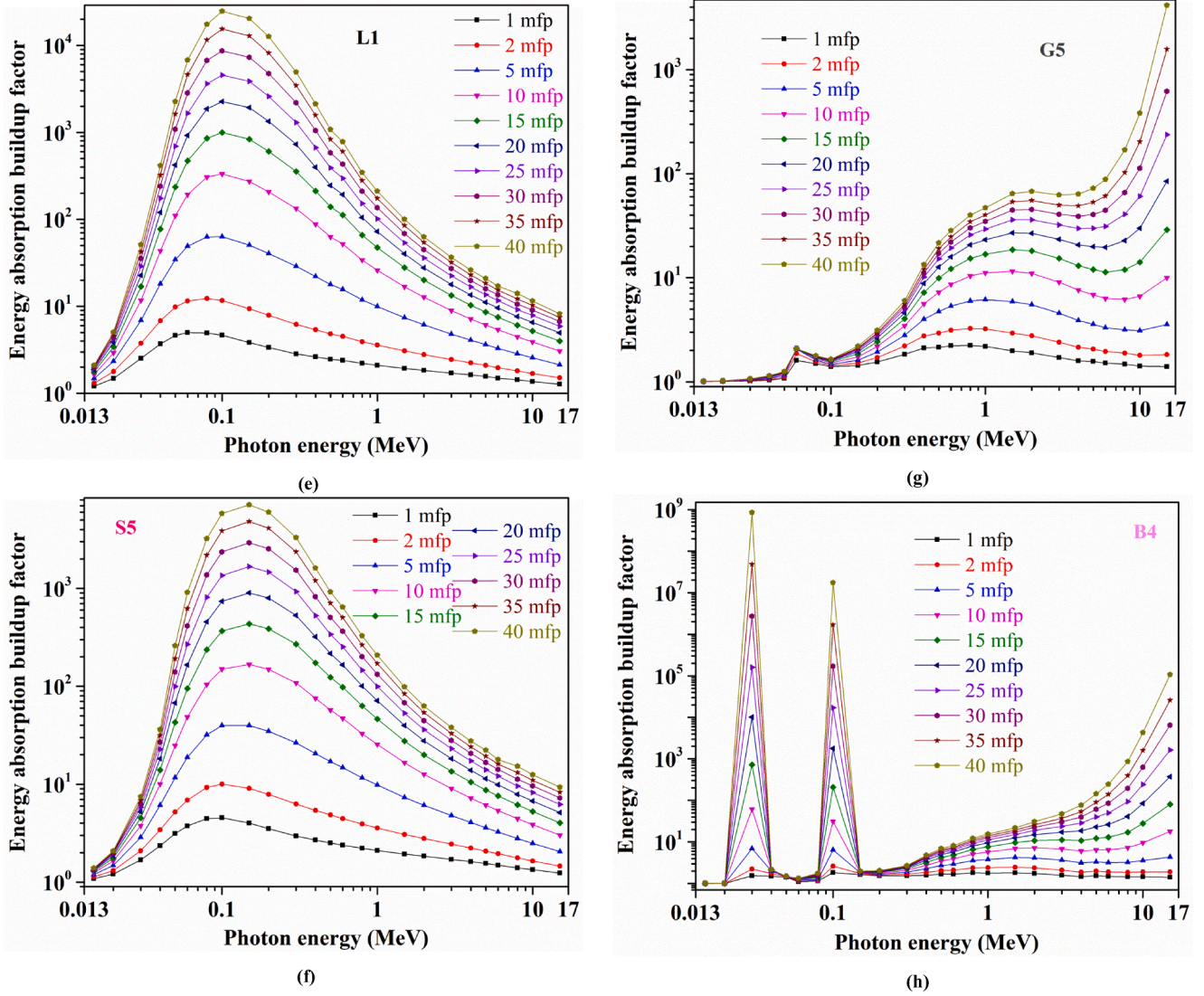
(e)

(g)

(f)

(h)

Fig. 15. (*continued*).

length between anion and cation) values are listed in Table 8. Likewise, Table 9 supplies G_i (per unit volume, dissociation energy), V_i (packing density factor), and CN values for all B_2O_3, Li_2O, Na_2O, K_2O, Gd_2O_3, SiO_2, Bi_2O_3, and ZnO oxides [78]. Following BC and M-M models, for all L1–L5, S1–S5, G1–G5, and B1–B4 samples, assessed corresponding K_{bc}, Y_{bc}, S_{bc}, L_{bc}, and σ_{cal} including $\overline{n}_c$ (average cross-link density), F, and n_b (per unit volume, number of network bonds), and Y_{M-M}, K_{M-M}, S_{M-M}, L_{M-M}, and σ_{M-M} along with G_t (total dissociation energy) and V_t (total ionic packing density) values are given in Tables 10–17. Principally, M-M model counts on each constituent compound's volumes and partial molar bonding energies. Connected with bond strength, Y_{bc} represents the stress and strain (linear) ratio, and σ indicates the ratio of deformation in a path at right angles to the loading direction in glasses. To estimate Y_{M-M}, K_{M-M}, S_{M-M}, L_{M-M}, and σ_{M-M}, first, V_t and G_t of considered oxide compositions are calculated.

From Table 10 data, one can notice that with Li_2O content rise in place of B_2O_3, all K_{bc}, Y_{bc}, S_{bc}, and L_{bc} quantities increase from sample L1 to L5. Here improvement in elastic moduli is owing to the increased connectivity with a higher number of bonds and rigidity. For L1–L5 glasses, K_{bc} values increased from 73.6381 to 89.893 GPa as K_{bc} varies following l (mean bond length), which relies on F and n_b [21]. The hike in Li_2O amount enhanced n_b from 5.63 to 8.47 ($\times 10^{28}$ m^{-3}) though F reduces from 608.27 to 464.19 N/m, hinting at the existence of the

structural modifications in samples' network. Further, $\overline{n}_c$ increases from 1.096 to 1.399, possibly because of the greater CN of Li_2O. Owing to such a rise in $\overline{n}_c$, σ_{cal} for L1–L5 samples decreased from 0.2737 to 0.2575. Values of Y_{bc}, S_{bc}, and L_{bc} are found to be increased from 99.9737 to 130.7991 GPa, from 39.2454 to 52.0076 GPa, and from 125.964 to 159.2347 GPa accordingly from sample L1 to L5. Next, following Table 11 data, from L1 to L5 glass, both V_t (from 0.5909 to 0.668) and G_t (from 21.5808 to 40.4577 kJ/cm^3) improved as Li_2O has a higher ionic radius and G_i (=77.9 kJ/cm^3) than B_2O_3 (=15.6 kJ/cm^3) (see Table 9). Similarly to V_t and G_i drift, all Y_{M-M}, K_{M-M}, S_{M-M}, and L_{M-M} quantities also increased from L1 to L5 glass, correspondingly varying at 106.6075–225.9352 GPa, 75.3521–180.532 GPa, 44.9668–93.1602 GPa, and 135.3063–304.7426 GPa spans with Li_2O incorporation. So, here one can identify the Li_2O positive effect on samples' rigidity with enhanced elastic constants. Obtained changes in elastic features could be ascribed to a greater number of NBOs (nonbridging oxygens) creation and an increase in defects in the network structure with Li_2O addition instead of B_2O_3 in L1–L5 samples. σ_{M-M} is 0.265, 0.272, 0.278, 0.289, and 0.292 individually for L1, L2, L3, L4, and L5 glasses with a rising trend. All elastic moduli (K, Y, S, and L) movements for L1–L5 samples are identical in BC and M-M models.

For S1–S5 samples, as can be identified from Table 12 data, both n_b and F values are reduced when Li_2O is gradually replaced by Na_2O at

Table 7

Formulae applied for elastic moduli calculations (i) Bond compression (BC) model and (ii) Makishima–Mackenzie (M-M) model.

(i) Bond compression (BC) model	
Force constant, F	$F = \dfrac{\sum_i (xn_f \bar{f})_i}{\sum_i (xn_f)_i}$ x = mole fraction of glass component oxide n_f = coordination number of cation $\bar{f}$ = stretching force constant
No. of network bonds per unit volume, n_b	$n_b = \dfrac{N_A}{V_m} \sum_i (xn_f)_i$ N_A = avogadro number V_m = molar volume
Average cross-link density, $\bar{n}_c$	$\bar{n}_c = \dfrac{1}{\eta} \sum_i (n_c)_i (N_c)_i$ η = total quantity of cations for each glass formula units n_c = number of cross-links per cation N_c = number of cations of each glass formula unit
Poisson's ratio, σ_{cal}	$\sigma_{cal} = 0.28(\bar{n}_c)^{-0.25}$ $\bar{n}_c$ = average cross-link density
Bulk modulus, K_{bc}	$K_{bc} = \dfrac{N_A}{9V_m} \sum_i (xn_f r^2)_i$ r = bond length between anion and cation (nm)
Shear modulus, S_{bc}	$S_{bc} = 1.5K_{bc} \dfrac{(1 - 2\sigma_{cal})}{(1 + \sigma_{cal})}$
Young's modulus, Y_{bc}	$Y_{bc} = 2S_{bc}(1 + \sigma_{cal})$
Longitudinal modulus, L_{bc}	$L_{bc} = K_{bc} + \dfrac{4}{3}S_{bc}$
(ii) Makishima–Mackenzie (M-M) model	
Total ionic packing density, V_t	$V_t = \dfrac{1}{V_m} \sum_i (V_i x_i)$ V_m = molar volume V_i = packing density factor of oxide x_i = mole fraction of glass component oxide
Total dissociation energy, G_t	$G_t = \sum_i (G_i x_i)$ G_i = dissociation energy per unit volume
Young's modulus, Y_{M-M}	$Y_{M-M} = 8.36 V_t G_t$
Bulk modulus, K_{M-M}	$K_{M-M} = 10 V_t^2 G_t$
Shear modulus, S_{M-M}	$S_{M-M} = \dfrac{3K_{M-M}}{(10.2V_t - 1)}$
Longitudinal modulus, L_{M-M}	$L_{M-M} = K_{M-M} + \left(\dfrac{4}{3}\right)S_{M-M}$
Poisson's ratio, σ_{M-M}	$\sigma_{M-M} = 0.5 - \left(\dfrac{1}{7.2V_t}\right)$

Table 8

Bond length between the anion and cation (r), stretching force constant (f), coordination number per cation (n_f), and cross-link density per cation (n_c) of B_2O_3, Li_2O, Na_2O, K_2O, Gd_2O_3, SiO_2, Bi_2O_3, and ZnO oxides.

Oxide	r (nm)	f (N/m)	n_f	$n_c = (n_f - 2)$
B_2O_3	0.138	660	3	1
Li_2O	0.159	243	4	2
Na_2O	0.196	225	4	2
K_2O	0.218	164	4	2
Gd_2O_3	0.242	147.5	6	4
SiO_2	0.1611	432	4	2
Bi_2O_3	0.240	216	3	1
ZnO	0.1988	219	6	4

constant K_2O and B_2O_3 amounts. Here n_b and F varied at 9.6423–7.6959 ($\times 10^{28}$ m^{-3}) and 412.6857–404.4571 N/m ranges from S1 to S5 glass, as Na_2O has lesser f value than Li_2O (see Table 8). Later, $\bar{n}_c$ exhibits an opposite drift to F and n_b, and changes at 1.6667 (sample S1) – 3 (glass S5) span. Further, K_{bc} value reduced with Na_2O content increment from glass S1 to S5 at 97.3422–87.4672 span. All Y_{bc}, S_{bc}, and L_{bc} quantities minorly only changed for S1–S5 samples, accordingly at 146.4294–150.7426 GPa, 59.4128–62.1367 GPa, and 170.1575–176.5573 GPa spans where glass S5 possesses the largest Y_{bc} and S_{bc}, and sample S1 owns the highest L_{bc}. Having inverse trend to $\bar{n}_c$ course, σ_{cal} varied at 0.2464 (sample S1) – 0.2128 (glass S5) range.

Table 9

Coordination number (CN), packing density factor (V_i), and dissociation energy per unit volume (G_i) of the oxides B_2O_3, Li_2O, Na_2O, K_2O, Gd_2O_3, SiO_2, Bi_2O_3, and ZnO.

Oxide	CN	V_i (cm^3/mol)	G_i (kJ/cm^3)
B_2O_3	3	20.8	15.6
Li_2O	–	8.0	77.9
Na_2O	–	11.2	31.9
K_2O	–	18.8	19.2
Gd_2O_3	7	24.9	68.8
SiO_2	–	14	68
Bi_2O_3	–	26.1	31.6
ZnO	6	7.9	49.9

Considering M-M model, from Table 13 data, from S1 to S5 sample, opposite to noticed L1–L5 glasses movement (Table 11), with Na_2O addition in place of Li_2O, both V_t and G_t reduced as Na_2O holds a lower G_i (=31.9 kJ/cm^3) than Li_2O (see Table 9). Next, following V_t and G_t trend, all Y_{M-M}, K_{M-M}, S_{M-M}, and L_{M-M} values also decreased from S1 to S5 sample, respectively changing at 241.998–114.9961 GPa, 204.9746–84.17 GPa, 98.8207–48.1762 GPa, and 336.7322–148.4033 GPa extents with Na_2O introduction in the glass network. So, here Na_2O effect on the rigidity of samples can be observed with varying Y_{M-M}, K_{M-M}, S_{M-M}, and L_{M-M} values. Later, with a reducing trend, σ_{M-M} value varied at 0.3039–0.273 range for S1–S5 samples.

For G1–G5 glasses, from Table 14 data, one can see that when both Gd_2O_3 and Si_2O contents increase in equal mol% in place of B_2O_3 amount, F value is regularly decreased from 392.5793 N/m to 327.75 N/m as such Gd_2O_3 (=147.5 N/m) and SiO_2 (=432 N/m) have lower f than B_2O_3 (=660 N/m) (see Table 8). Next, n_b varied minorly only from sample G1 to G5 at 7.0351–7.6933 ($\times 10^{28}$ m^{-3}) span. Contrary to the trend of F, $\bar{n}_c$ increased from 2.5172 to 3.4 from G1 to G5 glass. K_{bc} reduced from sample G1 to G3, and then increased for G4 and G5 glasses, where glass G3 has the lowest K_{bc} value (=81.526 GPa). Here K (bulk modulus) reflects the decrement in bulk volume of a glass, which arises when uniform forces are exerted on all sides of the glass. Generally, 'K' could be expressed as the ratio of applied pressure to the strain. Later, for G1–G5 samples, both Y_{bc} and S_{bc} enhanced with Gd_2O_3 and SiO_2 addition at 138.3494–152.9481 GPa and 56.5939–63.4008 GPa ranges accordingly. Likewise, L_{bc} varied at 158.3215 GPa (lowest, glass G3) – 171.7818 GPa (highest, sample G5) span for G1–G5 glasses. Showing an opposite movement to $\bar{n}_c$ values, σ_{cal} reduced at 0.2223–0.2062 extent for G1–G5 samples. Similarly, following Table 15 data, for G1–G5 glasses, V_t value varied slightly at 0.544–0.5715 range, where sample G1 has a higher V_t. Next, with improved Gd_2O_3 and SiO_2 amounts, G_t increased from 44.64 to 55.2 kJ/cm^3 as both Gd_2O_3 and SiO_2 possess bigger G_i, say, 68.8 kJ/cm^3 and 68 kJ/cm^3 separately than B_2O_3 (see Table 9). All Y_{M-M}, S_{M-M}, and L_{M-M} values increased from sample G1 to G5, changing at 213.2783–259.255 GPa, 90.5719–110.4917 GPa, and 266.5622–321.5441 GPa ranges accordingly. Here S (Shear modulus) could be obtained by a material's stress to strain (shear) ratio. Also, K_{M-M} varied at 145.7997–174.2218 GPa span, and for glasses G2 and G3 K_{M-M} value is insignificantly only deviated. σ_{M-M} is 0.257, 0.2517, 0.2447, 0.2515, and 0.2528 respectively for G1, G2, G3, G4, and G5 glasses with Gd_2O_3 and SiO_2 contents improvement in place of B_2O_3.

Following Table 16 data, at fixed ZnO and B_2O_3 mol% amount, when Li_2O is gradually substituted by Bi_2O_3, both n_b and F values are reduced as Bi_2O_3 has lower n_f and f (=216 N/m) than Li_2O (see Table 8). Here n_b and F quantities are varied at 4.2336–3.6188 ($\times 10^{28}$ m^{-3}) and 279.7714–277.791 N/m spans separately for B1–B4 glasses. Next, $\bar{n}_c$ increased from 3.743 to 5.75 with Bi_2O_3 addition. K_{bc} is decreased at 48.7767–45.856 GPa range from sample B1 to B4, whereas Y_{bc}, S_{bc}, and L_{bc} varied at 86.399–87.8314 GPa, 36.12–37.1915 GPa, and 95.4434–97.2107 GPa extents accordingly for such samples. Opposite to $\bar{n}_c$ trend, from B1 to B4 glass σ_{cal} reduced at 0.2017–0.1808 span. All

Table 10

Number of network bonds per unit volume (n_b), force constant, F (N/m), average cross-link density ($\bar{n}_c$), bulk modulus, K_{bc} (GPa), Young's modulus, Y_{bc} (GPa), shear modulus, S (GPa), longitudinal modulus, L (GPa), and Poisson's ratio (σ) values of all L1–L5 glasses.

Sample code	No. of network bonds per unit volume n_b ($\times10^{28}$ m^{-3})	Force constant, F	Average cross-link density, $\bar{n}_c$	K_{bc}	Y_{bc}	S_{bc}	L_{bc}	σ_{cal}
L1	5.630	608.2791	1.096	73.6381	99.9737	39.2454	125.9640	0.2737
L2	6.104	582.5912	1.146	77.1523	106.1955	41.7895	132.8702	0.2706
L3	6.621	556.2388	1.199	80.7072	112.5380	44.3902	139.8927	0.2676
L4	7.694	510.6646	1.295	87.7840	123.7615	48.9176	153.0058	0.2650
L5	8.470	464.1977	1.399	89.8930	130.7991	52.0076	159.2347	0.2575

Table 11

Total ionic packing density (V_t), total dissociation energy (G_t), Young's modulus, Y_{M-M} (GPa), bulk modulus, K_{M-M} (GPa), shear modulus, S_{M-M} (GPa), longitudinal modulus, L_{M-M} (GPa), and Poisson's ratio (σ_{M-M}) based on Makishima-Mackenzie model of all L1–L5 glasses.

Sample code	V_t	G_t	Y_{M-M}	K_{M-M}	S_{M-M}	L_{M-M}	σ_{M-M}
L1	0.5909	21.5808	106.6075	75.3521	44.9668	135.3063	0.2650
L2	0.6098	24.6958	125.8974	91.8328	52.7779	162.2016	0.2722
L3	0.6273	27.9977	146.8263	110.1724	61.2243	191.8028	0.2786
L4	0.660	33.9785	187.4798	148.0103	77.4653	251.2948	0.2896
L5	0.6680	40.4577	225.9352	180.5320	93.1602	304.7426	0.2921

Table 12

Number of network bonds per unit volume (n_b), force constant, F (N/m), average cross-link density ($\bar{n}_c$), bulk modulus, K_{bc} (GPa), Young's modulus, Y_{bc} (GPa), shear modulus, S (GPa), longitudinal modulus, L (GPa), and Poisson's ratio (σ) values of all S1–S5 glasses.

Sample code	No. of network bonds per unit volume n_b ($\times10^{28}$ m^{-3})	Force constant, F	Average cross-link density, $\bar{n}_c$	K_{bc}	Y_{bc}	S_{bc}	L_{bc}	σ_{cal}
S1	9.6423	412.6857	1.6667	97.3422	148.0975	59.4128	176.5573	0.2464
S2	9.2276	410.6286	1.875	96.0859	150.3087	60.6350	176.5506	0.2393
S3	8.4683	408.5714	2.1429	90.868	146.4294	59.4686	170.1575	0.2314
S4	8.1033	406.5143	2.5	89.5245	148.9639	60.9125	170.7391	0.2227
S5	7.6959	404.4571	3.0	87.4672	150.7426	62.1367	170.3141	0.2128

Table 13

Total ionic packing density (V_t), total dissociation energy (G_t), Young's modulus, Y_{M-M} (GPa), bulk modulus, K_{M-M} (GPa), shear modulus, S_{M-M} (GPa), longitudinal modulus, L_{M-M} (GPa), and Poisson's ratio (σ_{M-M}) based on Makishima-Mackenzie model of all S1–S5 glasses.

Sample code	V_t	G_t	Y_{M-M}	K_{M-M}	S_{M-M}	L_{M-M}	σ_{M-M}
S1	0.7081	40.88	241.9980	204.9746	98.8207	336.7322	0.3039
S2	0.6916	36.28	209.7628	173.5311	85.9871	288.1777	0.2992
S3	0.6476	31.68	171.5135	132.8614	71.1057	227.6666	0.2855
S4	0.632	27.08	143.0777	108.640	59.5792	187.6009	0.2802
S5	0.6119	22.48	114.9961	84.1700	48.1762	148.4033	0.273

Table 14

Number of network bonds per unit volume (n_b), force constant, F (N/m), average cross-link density ($\bar{n}_c$), bulk modulus, K_{bc} (GPa), Young's modulus, Y_{bc} (GPa), shear modulus, S (GPa), longitudinal modulus, L (GPa), and Poisson's ratio (σ) values of all G1–G5 glasses.

Sample code	No. of network bonds per unit volume n_b ($\times10^{28}$ m^{-3})	Force constant, F	Average cross-link density, $\bar{n}_c$	K_{bc}	Y_{bc}	S_{bc}	L_{bc}	σ_{cal}
G1	7.0351	392.5793	2.5172	83.03	138.3494	56.5939	158.4866	0.2223
G2	7.0761	375.2143	2.7143	82.5278	139.6021	57.3032	158.9302	0.2181
G3	7.0714	358.657	2.9259	81.5260	139.8597	57.5981	158.3215	0.2141
G4	7.4581	342.8523	3.1538	85.0311	147.8926	61.1076	166.5059	0.2101
G5	7.6933	327.75	3.4	86.7732	152.9481	63.4008	171.7818	0.2062

Table 15

Total ionic packing density (V_t), total dissociation energy (G_t), Young's modulus, Y_{M-M} (GPa), bulk modulus, K_{M-M} (GPa), shear modulus, S_{M-M} (GPa), longitudinal modulus, L_{M-M} (GPa), and Poisson's ratio (σ_{M-M}) based on Makishima-Mackenzie model of all G1–G5 glasses.

Sample code	V_t	G_t	Y_{M-M}	K_{M-M}	S_{M-M}	L_{M-M}	σ_{M-M}
G1	0.5715	44.64	213.2783	145.7997	90.5719	266.5622	0.257
G2	0.5593	47.28	221.0694	147.8996	94.3065	273.6416	0.2517
G3	0.544	49.92	227.0282	147.7312	97.4309	277.6391	0.2447
G4	0.5589	52.56	245.5815	164.1812	104.7791	303.8867	0.2515
G5	0.5618	55.2	259.2550	174.2218	110.4917	321.5441	0.2528

Table 16

Number of network bonds per unit volume (n_b), force constant, F (N/m), average cross-link density ($\bar{n}_c$), bulk modulus, K_{bc} (GPa), Young's modulus, Y_{bc} (GPa), shear modulus, S (GPa), longitudinal modulus, L (GPa), and Poisson's ratio (σ) values of all B1–B4 glasses.

Sample code	No. of network bonds per unit volume n_b ($\times 10^{28}$ m^{-3})	Force constant, F	Average cross-link density, $\bar{n}_c$	K_{bc}	Y_{bc}	S_{bc}	L_{bc}	σ_{cal}
B1	4.2336	279.7714	3.743	48.7767	87.3069	36.3264	97.2107	0.2017
B2	3.9823	279.1304	4.1667	47.3643	86.3990	36.1200	95.5231	0.1960
B3	3.8312	278.4706	4.8	47.0362	87.7123	36.8787	96.2066	0.1892
B4	3.6188	277.7910	5.75	45.8560	87.8314	37.1915	95.4434	0.1808

Table 17

Total ionic packing density (V_t), total dissociation energy (G_t), Young's modulus, Y_{M-M} (GPa), bulk modulus, K_{M-M} (GPa), shear modulus, S_{M-M} (GPa), longitudinal modulus, L_{M-M} (GPa), and Poisson's ratio (σ_{M-M}) based on Makishima-Mackenzie model of all B1–B4 glasses.

Sample code	V_t	G_t	Y_{M-M}	K_{M-M}	S_{M-M}	L_{M-M}	σ_{M-M}
B1	0.3989	40.29	134.3593	64.1099	62.6730	147.6718	0.1519
B2	0.3981	37.975	126.3852	60.1842	58.9922	138.8385	0.1511
B3	0.4055	35.66	120.8867	58.6358	56.0911	133.4221	0.1575
B4	0.4050	33.345	112.8995	54.6941	52.4057	124.5666	0.1570

such changes in elastic moduli reveal structural modifications in B1–B4 glasses network in terms of rigidity. Further, from Table 17 data, from B1 to B4 sample, calculated V_t value is changed minorly only at 0.3981–0.4055 range. Next, G_t reduced from 40.29 to 33.345 kJ/cm^3 as Bi$_2$O$_3$ possesses a lower G_i (=31.6 kJ/cm^3) than Li$_2$O (see Table 9). Likewise, with improved Bi$_2$O$_3$ from B1 to B4 glass, all Y_{M-M}, K_{M-M}, S_{M-M}, and L_{M-M} values decreased, varying at 134.3593–112.8995 GPa, 64.1099–54.6941 GPa, 62.673–52.4057 GPa, and 147.6718–124.5666 GPa ranges correspondingly. σ_{M-M} insignificantly altered for B1–B4 samples at 0.1511–0.1575 span.

Recently, for different borate-based glass systems, antibacterial [79], gamma-ray shielding [80], and gamma irradiation [81] features were studied and reported by other researchers.

Conclusions

Elastic aspects and nuclear radiation attenuation factors of four types of cheaper borate-based glass systems in the composition B$_2$O$_3$-Li$_2$O, Li$_2$O-Na$_2$O-K$_2$O-B$_2$O$_3$, Gd$_2$O$_3$-SiO$_2$-B$_2$O$_3$, and Bi$_2$O$_3$-Li$_2$O-ZnO-B$_2$O$_3$ coded as L1–L5, S1–S5, G1–G5, and B1–B4 respectively were investigated. With Li$_2$O content rise in place of B$_2$O$_3$, all Y_{M-M}, K_{M-M}, S_{M-M}, and L_{M-M} values improved from L1 to L5 sample, individually changing at 106.6–225.9 GPa, 75.3–180.5 GPa, 44.96–93.16 GPa, and 135.3–304.7 GPa extents, whereas all K_{bc}, Y_{bc}, S_{bc}, and L_{bc} quantities also enhanced from glass L1 to L5. Next, all Y_{bc}, S_{bc}, and L_{bc} minorly only varied for S1–S5 glasses, correspondingly at 146.42–150.74 GPa, 59.41–62.13 GPa, and 170.15–176.55 GPa ranges where sample S5 has the highest Y_{bc} and S_{bc}, and glass S1 possesses the largest L_{bc}. But, all Y_{M-M}, K_{M-M}, S_{M-M}, and L_{M-M} values reduced from S1 to S5 sample, accordingly varying at 241.99–114.99 GPa, 204.97–84.17 GPa, 98.82–48.17 GPa, and 336.73–148.4 GPa spans with Na$_2$O substitution instead of Li$_2$O in the composition. For G1–G5 glasses, when both Gd$_2$O$_3$ and Si$_2$O amounts improved in equal mol% in place of B$_2$O$_3$ content, σ_{cal} reduced at 0.2223–0.2062 range and all Y_{M-M}, S_{M-M}, and L_{M-M} values increased from glass G1 to G5, fluctuating at 213.27–259.25 GPa, 90.57–110.49 GPa, and 266.56–321.54 GPa extents separately. Later, at constant ZnO and B$_2$O$_3$ contents, when Li$_2$O is gradually replaced by Bi$_2$O$_3$, K_{bc} reduced at 48.77–45.85 GPa range from glass B1 to B4, while Y_{bc}, S_{bc}, and L_{bc} changed at 86.39–87.83 GPa, 36.12–37.19 GPa, and 95.44–97.21 GPa spans respectively. Further, σ_{M-M} is negligibly varied for B1–B4 samples at 0.1511–0.1575 extent. For fast neutrons, sample S1 (Li: 9.8836 wt%, K: 13.9191 wt%, B: 19.2429 wt%, and O: 56.9544 wt%) has higher Σ_R (=0.11755 cm^{-1}) in all studied glasses, owning ρ = 2.57 g/cm^3, and also its Σ_R is identified to be higher than those of Graphite (=0.0773 cm^{-1}), H$_2$O (=0.1023 cm^{-1}), and ordinary concrete

(=0.0937 cm^{-1}). Likewise, sample G5 (Gd: 67.0585 wt%, Si: 5.9885 wt%, B: 3.0736 wt%, and O: 23.8794 wt%) possesses a superior ability for thermal neutron absorption, having ρ = 4.993 g/cm^3, whereas glass B4 (ρ = 6.21 g/cm^3) exhibits minimal σ_T in all glasses. Additionally, glass G5 retains a larger SP at minimal 't' for thermal energy neutrons. γ-ray shielding prowess in terms of μ, μ/ρ, Z_{eff}, N_{eff}, HVL, TVL, MFP, RPE, Z_{eq}, EBF, EABF were examined at energy 15 keV–15 MeV span. Specifically, Phy-X/PSD and WinXCOM programs along with Geant4, FLUKA, PHITS, and MCNPX codes were operated to validate μ/ρ values of glass B4 as in all glasses such sample holds relatively a higher μ/ρ across all energies considered. For G1–G5 or B1–B4 glasses, Gd$_2$O$_3$ or Bi$_2$O$_3$ addition in place of B$_2$O$_3$ or Li$_2$O improved μ/ρ, μ, and Z_{eff} considerably, where sample B4 has the largest Z_{eff}. Usually, high-Z elements incorporation increases the number of the net electrons in glass for greater interactions' occurrence with incoming photons. Furthermore, B4 glass holds the lowest MFP, TVL, and HVL for any tested energy. It is found that to reduce 662 keV γ-rays intensity to ½, ~1.327 times lower 't' glass B4 is sufficient than RS 520 glass. In all selected glasses, sample B4 showed larger RPE and lesser BUFs owing to its higher Z and ρ, where EABFs and EBFs have primarily relied on composition and Z_{eq}. PP, CS, and PEA mechanisms' dominances were noticed individually at higher, intermediate, and minimal energy extents for different photon interaction factors' variations. In all chosen glasses, sample B4 possesses higher Z_{eq} changing at 42.94 (minimal, for 40 keV) – 76.18 (largest, for 1 MeV). Such outcomes specify that glass B4 (Bi: 84.4986 wt%, Li: 0.2005 wt%, Zn: 1.8883 wt%, B: 0.9367 wt%, and O: 12.4759 wt%) has a better potential for γ-rays attenuation than all explored glasses for its possible utilization as a shield at radiation environments in place of standard concrete and toxic lead-based materials.

CRediT authorship contribution statement

G. Lakshminarayana: Conceptualization, Visualization, Writing – original draft, Writing – review & editing, Supervision. **H.O. Tekin:** Software, Formal analysis, Data curation. **M.G. Dong:** Formal analysis, Validation, Data curation. **M.S. Al-Buriahi:** Software, Formal analysis, Data curation. **Dong-Eun Lee:** Project administration, Funding acquisition, Supervision. **Jonghun Yoon:** Validation, Supervision. **Taejoon Park:** Project administration, Funding acquisition, Supervision.

Declaration of Competing Interest

Acknowledgements

Appendix A. Supplementary data

MCNPX simulation setup (3-D view, obtained from Visual Editor of MCNPX) for mass attenuation coefficients computation of all selected glasses and MCNPX simulation setup (2-D view) for μ/ρ calculations acquired from MCNPX Visual Editor (version X_22S) (Fig. S1), diagrams of principle simulation geometry utilized for PHITS, FLUKA, and Geant4 codes (Fig. S2), variation of linear attenuation coefficient with photon energy for all L1–L5, S1–S5, and G1–G5 glasses (Figs. S3–S5), variation of effective atomic number with photon energy for all L1–L5, S1–S5, G1–G5, and B1–B4 glasses (Figs. S6–S9), variation of effective electron density with photon energy for all L1–L5, S1–S5, G1–G5, and B1–B4 glasses (Figs. S10–S13), variation of radiation protection efficiency with photon energy for all L1–L5, S1–S5, and G1–G5 glasses (Figs. S14–S16), variation of equivalent atomic number with photon energy for L1, S5, G5, and B4 samples (Fig. S17), coherent scattering cross-section (σ_{cs}, barn), incoherent scattering cross-section (σ_{ics}, barn), absorption cross-section (σ_A, barn), and total cross-section (σ_T, barn) of B, Li, Na, K, Gd, Si, Bi, Zn, and O elements for thermal neutrons (Table S1), mass attenuation coefficients of all L1–L5, S1–S5, G1–G5, and B1–B4 glasses estimated using MCNPX code (Table S2), and mass attenuation co-efficients of glass B4 estimated using WinXCOM program and PHITS, FLUKA, and Geant4 codes including relative difference (RD, %) values among them (Table S3) Supplementary data to this article can be found online at https://doi.org/10.1016/j.rinp.2022.105527.

References

[1] Al Nabhani K. *5 – Application of nuclear science and radioisotopes technology in the sustainability of agriculture and water resources, and food safety*, Al Nabhani K. Applications of Nuclear and Radioisotope Technology, Academic Press, 2021. pp. 159–185. ISBN 9780128213193. https://doi.org/10.1016/B978-0-12-821319-3.00006-3.

[2] Firouzi S, Khorshidi A, Nabipour JS, Barzi SMZ, Amani M, Ay MR. Evaluation of gamma and electron radiations impact on vitamins for onion preservation. Appl Radiat Isot 2021;167:109442.

[3] Piron S, Verhoeven J, Vanhove C, Vos FD. Recent advancements in ^{18}F-labeled PSMA targeting PET radiopharmaceuticals. Nucl Med Biol 2022;106–107:29–51.

[4] Hassanpour SH, Vafapour H, Karami SZ. The presentation of clinical results of radiolabelling of ^{99m}Tc-MIBI complex using ultrasound technique for myocardial perfusion SPECT scanning. Méd Nucléaire 2021;45(5-6):271–8.

[5] Fushiki S. Radiation hazards in children – lessons from Chernobyl, Three Mile Island and Fukushima. Brain Dev 2013;35(3):220–7.

[6] Ding Y, Long X, Peng S, Zhang D, Tan Z, Lu X. Phase evolution and aqueous durability of $Zr_{1-x-y}Ce_xNd_yO_{2-y/2}$ ceramics designed to immobilize actinides with multi-valences. J Nucl Mater 2017;487:297–304.

[7] Tamayo P, Thomas C, Rico J, Pérez S, Mananes A. Radiation shielding properties of siderurgical aggregate concrete. Constr Build Mater 2022;319:126098.

[8] Lee S-W, Ahn J-H, Moon B-M, Kim DE, Oh SK, Kim Y-J, et al. Preliminary study on Fe-Gd alloys as binary alloys and master alloys for potential spent nuclear fuel (SNF) application. Mater Des 2020;194:108906.

[9] Lee C-M, Lee YH, Lee KJ. Cracking effect on gamma-ray shielding performance in concrete structure. Prog Nucl Energy 2007;49(4):303–12.

[10] Gencel O. Effect of elevated temperatures on mechanical properties of high-strength concrete containing varying proportions of hematite. Fire Mater 2012;36(3):217–30.

[11] Lakshminarayana G, Issa SAM, Saddeek YB, Tekin HO, Al-Buriahi MS, Dong MG, et al. Analysis of physical and mechanical traits and nuclear radiation transmission aspects of Gallium(III) trioxide constituting Bi_2O_3-B_2O_3 glasses. Results Phys 2021;30:104899.

[12] Körpınar B, Öztürk BC, Çam NF, Akat H. Investigations on thermal and radiation shielding properties of the poly(hydroxyethyl methacrylate-co-styrene)/tungsten (VI) oxide composites. Prog Nucl Energy 2020;126.

[13] Cherkashina NI, Pavlenko VI, Noskov AV, Sirota VV, Zaitsev SV, Prokhorenkov DS, et al. Gamma radiation attenuation characteristics of polyimide composite with WO_2. Prog Nucl Energy 2021;137:103795.

[14] Turhan MF, Akman F, Taşer A, Dilsiz K, Oğul H, Kaçal MR, et al. Gamma radiation shielding performance of $Cu_xAg_{(1-x)}$-alloys: Experimental, theoretical and simulation results. Prog Nucl Energy 2022;143:104036.

[15] Aygün B. Neutron and gamma radiation shielding Ni based new type super alloys development and production by Monte Carlo Simulation technique. Radiat Phys Chem 2021;188:109630.

[16] Eid EA, Sadawy MM, Reda AM. Computing the dynamic friction coefficient and evaluation of radiation shielding performance for AISI 304 stainless steel. Mater Chem Phys 2022;277:125446.

[17] Sadawy MM, El Shazly RM. Nuclear radiation shielding effectiveness and corrosion behavior of some steel alloys for nuclear reactor systems. Defence Technol 2019;15(4):621–8.

[18] Aygün B, Şakar E, Korkut T, Sayyed MI, Karabulut A, Zaid MHM. Fabrication of Ni, Cr, W reinforced new high alloyed stainless steels for radiation shielding applications. Results Phys 2019;12:1–6.

[19] Luo H, Li Y, Xiang R, Jia W, Li M, Li S, et al. Exploring the potential of the mechanical/thermal properties and co-shielding ability of Bi_2O_3-doped aluminum borate ceramics against neutron/gamma radiation. Ceram Int 2021;47(11):15508–19.

[20] Temir A, Zhumadilov K, Zdorovets M, Kozlovskiy A, Trukhanov A. Study of gamma radiation shielding efficiency with radiation-resistant Bi_2O_3-TeO_2-WO_3 ceramics. Solid State Sci 2021;115:106604.

[21] Lakshminarayana G, Kumar A, Tekin HO, Issa SAM, Al-Buriahi MS, Dong MG, et al. Illustration of distinct nuclear radiation transmission factors combined with physical and elastic characteristics of barium boro-bismuthate glasses. Results Phys 2021;31:105067.

[22] El-Denglawey A, Issa SAM, Saddeek YB, Elshami W, Sayed MA, Elsaman R, et al. Mechanical, structural and nuclear radiation shielding competencies of some tellurite glasses reinforced with molybdenum trioxide. Phys Scr 2021;96:045702.

[23] Alrowaili ZA, Taha TA, Ibrahim M, Saron KMA. Investigation of the structure and radiation shielding properties of borate/Y_2O_3 glasses. Eur Phys J Plus 2021;136:567.

[24] Kavaz E, El-Agawany FI, Tekin HO, Perisanoglu U, Rammah YS. Nuclear radiation shielding using barium borosilicate glass ceramics. J Phys Chem Solids 2020;142:109437.

[25] Rammah YS, Olarinoye IO, El-Agawany FI, El-Adawy A, Yousef ES. Environment friendly La^{3+} ions doped phosphate glasses/glass-ceramics for gamma radiation shielding: Their potential in nuclear safety applications. Ceram Int 2020;46:27616–26.

[26] Bengisu M. Borate glasses for scientific and industrial applications: a review. J Mater Sci 2016;51:2199–242.

[27] Ojovan MI, Lee WE. *Chap. 17 – Immobilisation of Radioactive Wastes in Glass*, in An Introduction to Nuclear Waste Immobilisation. 2005. Pages 213–249. ISBN 978-0-08-044462-8. https://doi.org/10.1016/B978-0-08-044462-8.X5000-5.

[28] Piovesan V, Bardez-Giboire I, Fournier M, Frugier P, Jollivet P, Montouillout V, et al. Chemical durability of peraluminous glasses for nuclear waste conditioning. npj Mater Degrad 2018;2(1).

[29] Sears VF. Neutron scattering lengths and cross sections. Neutron News 1992;3(3):26–37.

[30] Lee GH, Chang Y, Kim T-J. Ultrasmall lanthanide oxide nanoparticles for biomedical imaging and therapy. Woodhead Publishing; 2014.

[31] Castley D, Goodwin C, Liu J. Computational and experimental comparison of boron carbide, gadolinium oxide, samarium oxide, and graphene platelets as additives for a neutron shield. Radiat Phys Chem 2019;165:108435.

[32] Dumazert J, Coulon R, Lecomte Q, Bertrand GHV, Hamel M. Gadolinium for neutron detection in current nuclear instrumentation research: A review. Nucl Instrum Methods Phys Res Sect A: Accel Spectrom Detect Assoc Equip 2018;882:53–68.

[33] Kandlakunta P, Cao LR, Mulligan P. Measurement of internal conversion electrons from Gd neutron capture. Nucl Instrum Methods Phys Res Sect A: Accel Spectrom Detect Assoc Equip 2013;705:36–41.

[34] Wang W, Zhang J, Wan S, Zhang T. Design, fabrication and comprehensive properties of the novel thermal neutron shielding Gd/316L composites. Fusion Eng Des 2021;171:112566.

[35] Xu ZG, Jiang LT, Zhang Q, Qiao J, Gong D, Wu GH. The design of a novel neutron shielding B_4C/Al composite containing Gd. Mater Des 2016;111:375–81.

[36] Dubuis S, Messaddeq SH, Ledemi Y, Côté A, Messaddeq Y. Effect of B_2O_3 on the physical, structural and NIR emission properties of BGG glasses prepared using different melting atmospheres. Opt Mater Express 2021;11:2560–75.

[37] Colak SC, Akyuz I, Atay F. On the dual role of ZnO in zinc-borate glasses. J Non-Cryst Solids 2016;432:406–12.

[38] Mahmoud M, Makhlouf SA, Alshahrani B, Yakout HA, Shaaban KS, Wahab EAA. Experimental and Simulation investigations of mechanical properties and gamma radiation shielding of lithium cadmium gadolinium silicate glasses doped erbium ions. Silicon 2022;14(6):2905–19.

[39] Kaewnuam E, Wantana N, Tanusilp S, Kurosaki K, Limkitjaroenporn P, Kaewkhao J. The influence of Gd_2O_3 on shielding, thermal and luminescence properties of WO_3-Gd_2O_3-B_2O_3 glass for radiation shielding and detection material. Radiat Phys Chem 2022;190:109805.

[40] Stalin S, Edukondalu A, Boukhris I, Alrowaili ZA, Al-Baradi AM, Olarinoye IO, et al. Effects of TeO_2/B_2O_3 substitution on synthesis, physical, optical and radiation shielding properties of ZnO-Li_2O-GeO_2-Bi_2O_3 glasses. Ceram Int 2021;47(21):30137–46.

[41] Saudi HA, Tekin HO, Zakaly HMH, Issa SAM, Susoy G, Zhukovsky M. The impact of samarium (III) oxide on structural, optical and radiation shielding properties of thallium-borate glasses: Experimental and numerical investigation. Opt Mater 2021;114:110948.

[42] Saleh EE, Algradee MA, Al-Fakeh MS. Nuclear radiation shielding behavior for prepared LNZP glasses doped with (CdO+Te). Radiat Phys Chem 2021;189: 109743.

[43] Zaid MHM, Matori KA, Sidek HAA, Ibrahim IR. Bismuth modified gamma radiation shielding properties of titanium vanadium sodium tellurite glasses as a potent transparent radiation-resistant glass applications. Nucl Eng Technol 2021;53(4): 1323–30.

[44] Rammah YS, Mutuwong C, Yousef ES, Alraddadi S, Al-Buriahi MS. Gamma-ray/ neutron shielding capacity and elastic moduli of MnO–K$_2$O–B$_2$O$_3$ glasses co-doped with Er^{3+} ions. Appl Phys A 2020;126:929.

[45] Rammah YS, Ahmed EM, Elshami W, Tekin HO. Mechanical properties and elastic moduli, as well as gamma-ray attenuation abilities: A wide-ranging investigation into calcium/ sodium/phosphate glasses. J Aust Ceram Soc 2021;57:1309–19.

[46] Malidarre RB, Akkurt I, Kavas T. Monte Carlo simulation on shielding properties of neutron-gamma from ^{252}Cf source for alumino-boro-silicate glasses. Radiat Phys Chem 2021;186:109540.

[47] Aladailah MW, Tashlykov OL, Shirmanov IA, Strugov ED, Marashdeh MW, Abdelmunem EM, et al. Photon absorption capabilities of SiO$_2$–Na$_2$O–P$_2$O$_5$–CaO–MgO glasses. Radiat Phys Chem 2022;190:109814.

[48] Alharshan GA, Eke C, Al-Buriahi MS. Radiation-transmission and self-absorption factors of P$_2$O$_5$–SrO–Sb$_2$O$_3$ glass system. Radiat Phys Chem 2022;193:109938.

[49] Abouhaswa AS, Tekin HO, Araz A, Kavaz E. Refinement of optical/structural features and neutron/gamma-ray protecting capability of P$_2$O$_5$–Li$_2$O–BaO phosphate glass system by adding Bi$_2$O$_3$. Prog Nucl Energy 2022;145:104114.

[50] Bridge B, Higazy A. A model of the compositional dependence of the elastic moduli of polycomponent oxide glasses. Phys Chem Glasses 1986;27:1–14.

[51] Bridge B, Patel ND, Waters DN. On the elastic constants and structure of the pure inorganic oxide glasses. Phys Status Solidi 1983;77(2):655–68.

[52] Abd El-Moneim A. Bond compression bulk modulus and Poisson's ratio of the polycomponent silicate glasses. Mater Chem Phys 2001;70(3):340–3.

[53] Makishima A, Mackenzie JD. Direct calculation of Young's modulus of glass. J Non-Cryst Solids 1973;12:35–45.

[54] Makishima A, Mackenzie JD. Calculation of bulk modulus, shear modulus and Poisson's ratio of glass. J Non-Cryst Solids 1975;17(2):147–57.

[55] Makehima A, Tamura Y, Sakaino T. Elastic moduli and refractive indices of aluminosilicate glasses containing Y$_2$O$_3$, La$_2$O$_3$, and TiO$_2$. J Am Ceram Soc 1978;61 (5-6):247–9.

[56] RSICC Computer Code Collection, MCNPX User's Manual Version 2.4.0. Monte Carlo N-Particle Transport Code System for Multiparticle and High Energy Applications; 2004.

[57] Şakar E, Özpolat ÖF, Alım B, Sayyed MI, Kurudirek M. Phy-X/PSD: Development of a user friendly online software for calculation of parameters relevant to radiation shielding and dosimetry. Radiat Phys Chem 2020;166:108496.

[58] Sørensen SS, Johra H, Mauro JC, Bauchy M, Smedskjaer MM. Boron anomaly in the thermal conductivity of lithium borate glasses. Phys Rev Mater 2019;3:075601.

[59] Samee MA, Awasthi AM, Shripathi T, Bale S, Srinivasu Ch, Rahman S. Physical and optical studies in mixed alkali borate glasses with three types of alkali ions. J Alloys Compd 2011;509(6):3183–9.

[60] Luo H, Hu X, Liu W, Zhang Y, Lu A, Hao X. Compositional dependence of properties of Gd$_2$O$_3$–SiO$_2$–B$_2$O$_3$ glasses with high Gd$_2$O$_3$ concentration. J Non-Cryst Solids 2014;389:86–92.

[61] Bale S, Purnima M, Srinivasu Ch, Rahman S. Vibrational spectra and structure of bismuth based quaternary glasses. J Alloys Compd 2008;457(1-2):545–8.

[62] Gerward L, Guilbert N, Jensen KB, Levring H. WinXCom—a program for calculating X-ray attenuation coefficients. Radiat Phys Chem 2004;71(3-4):653–4.

[63] Sato T, Iwamoto Y, Hashimoto S, Ogawa T, Furuta T, Abe S-I, et al. Features of particle and heavy ion transport code system (PHITS) version 3.02. J Nucl Sci Technol 2018;55(6):684–90.

[64] Ballarini F, Battistoni G, Brugger M, Campanella M, Carboni M, Cerutti F, et al. The physics of the FLUKA code: Recent developments. Adv Space Res 2007;40(9): 1339–49.

[65] Battistoni G, Boehlen T, Cerutti F, Chin PW, Esposito LS, Fassò A, et al. Overview of the FLUKA code. Ann Nucl Energy 2015;82:10–8.

[66] Agostinelli S, Allison J, Amako K, Apostolakis J, Araujo H, Arce P, et al. GEANT4-A simulation toolkit. Nucl Instrum Methods Phys Res Sect A: Accel Spectrometers, Detect Assoc Equip 2003;506(3):250–303.

[67] Allison J, Amako K, Apostolakis J, Araujo H, Arce Dubois P, Asai M, et al. Geant4 developments and applications. IEEE Trans Nucl Sci 2006;53(1):270–8.

[68] Allison J, Amako K, Apostolakis J, Arce P, Asai M, Aso T, et al. Recent developments in Geant4. Nucl Instrum Methods Phys Res Sect A: Accel Spectrometers, Detect Assoc Equip 2016;835:186–225.

[69] Al-Buriahi MS, Abouhaswa AS, Tekin HO, Sriwunkum C, El-Agawany FI, Nutaro T, et al. Structure, optical, gamma-ray and neutron shielding properties of NiO doped B$_2$O$_3$–BaCO–Li$_2$O$_3$ glass systems. Ceram Int 2020;46(2):1711–21.

[70] Shibayama M, Jinnai H, Hashimoto T. Chap. 2 - Neutron Scatterin. In: Tanaka T, editor. Polymers, Interfaces and biomaterials, experimental methods in polymer science. Elsevier; 2000. p. 57–154.

[71] Bryan JC. Introduction to nuclear science. Boca Raton, Florida, USA: CRC Press; 2009. p. 161.

[72] El Abd A, Mesbah G, Mohammed NMA, Ellithi A. A simple method for determining the effective removal cross section for fast neutrons. J Rad Nucl Appl 2016;2(2): 53–8.

[73] Bashter II. Calculation of radiation attenuation coefficients for shielding concretes. Ann Nucl Energy 1997;24(17):1389–401.

[74] Lakshminarayana G, Kumar A, Tekin HO, Issa SAM, Al-Buriahi MS, Dong MG, et al. Probing of nuclear radiation attenuation and mechanical features for lithium bismuth borate glasses with improving Bi$_2$O$_3$ content for B$_2$O$_3$+Li$_2$O amounts. Results Phys 2021;25:104246.

[75] ML11229A721 – 0751 – H122 – Basic Health Physics – 32 – Shielding Radiation. (112 pages, 7/5/2011).

[76] https://www.schott.com/d/advanced_optics/352fbb5f-4d56-49d3-bb47-256437d58f0a/1.4/schott-radiation-shielding-glass-may-2013-eng.pdf. (Accessed January 2022).

[77] Tekin HO, ALMisned G, Susoy G, Zakaly HMH, Issa SAM, Kilic G, et al. A detailed investigation on highly dense CuZr bulk metallic glasses for shielding purposes. Open Chem 2022;20(1):69–80.

[78] Inaba S, Fujino S, Morinaga K. Young's modulus and compositional parameters of oxide glasses. J Am Ceram Soc 1999;82:3501–7.

[79] Abdallah EM, Meikhail MS, El-Adawy A, Othman HA, Abdelghany AM. Structural and antibacterial peculiarities of modified borate bioglass containing mixed dopant oxides. J Bio- Tribo-Corros 2022;8(39):1–11.

[80] Abdelghany AM, Rammah YS. Transparent alumino lithium borate glass-ceramics: synthesis, structure and gamma-ray shielding attitude. J Inorg Organomet Polym Mater 2021;31(6):2560–8.

[81] Abdelghany AM, ElBatal HA, EzzElDin FM. Influence of CuO content on the structure of lithium fluoroborate glasses: spectral and gamma irradiation studies. Spectrochim Acta A Mol Biomol Spectrosc 2015;149:788–92.